

CR-137818

ATR-74-16-1

COMPUTATION OF STEADY AXISYMMETRIC FLOW USING
A ONE-DIMENSIONAL TIME-DEPENDENT METHOD

prepared by

Leonard Walitt

for

AMES RESEARCH CENTER
National Aeronautics and Space Administration
Moffett Field, California

The work reported herein was performed
under Contract NAS2-4998

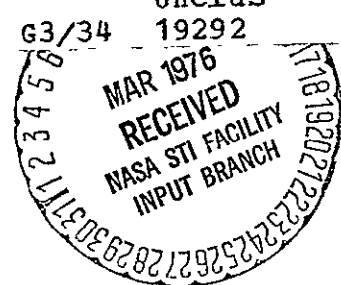
(NASA-CR-137818) COMPUTATION OF STEADY
AXISYMMETRIC FLOW USING A ONE-DIMENSIONAL
TIME-DEPENDENT METHOD (Applied Theory, Inc.)
61 p HC \$4.50

CSCL 20D

N76-19369

Unclass

19292



August 1974

APPLIED THEORY, INC.
1010 Westwood Boulevard
Los Angeles, California 90024

ACKNOWLEDGEMENTS

The author is pleased to acknowledge the contributions of Dr. J. G. Trulio of Applied Theory, Inc., Professor C. Y. Liu of the University of California at Los Angeles, and Mr. L. S. King of NASA Ames Research Center to the work reported herein. Dr. Trulio suggested that solutions to the full Navier-Stokes equations be sought by iteration; thus, changing the direction of the entire program. It was initially intended to drop axial elliptic terms from the Navier-Stokes equations and develop approximate solutions. Professor Liu developed the Lagrangian computer code which was used for the inviscid flow calculations and selected the cone-cylinder-flare problem for numerical investigation. Mr. King provided many helpful suggestions and discussions in the course of this work.

TABLE OF CONTENTS

<u>SECTION</u>		<u>PAGE</u>
	ABSTRACT	i
	NOMENCLATURE	ii
1	INTRODUCTION	1
2	THE NUMERICAL METHOD	4
	2.1 General Description of the Iteration Technique for Axisymmetric Flow	4
	2.2 Formulation of the Finite Difference Equations for Axisymmetric Flow	6
	2.3 Total Energy Conservation and Stability of the Finite Difference Equations	12
3	RESULTS OF CALCULATIONS FOR A CONE-CYLINDER- FLARE BODY	14
	3.1 General Description of Problem	14
	3.2 Mesh Boundary Conditions, and Initial Conditions Used	16
	3.3 Zeroth Iterate: The Inviscid Flow Field	17
	3.4 First, Second and Third Iterates: The Viscous Flow Field	19
	3.4.1 Flow Field and Pressure Distribution	20
	3.4.2 The Cone Boundary Layer for Infinite Prandtl Number	21
	3.5 Separation at the Cylinder-Flare Junction	23
4	CONCLUSIONS	25
	APPENDIX A	27
	APPENDIX B	31
	APPENDIX C	38
	REFERENCES	54

ABSTRACT

An iterative numerical method is studied for computing steady, three-dimensional, viscous, compressible flow fields about aerodynamic bodies. In order to develop the iterative method economically, the primary emphasis of this research was directed towards supersonic, axisymmetric flow. However, the technique readily extends to three spatial dimensions. The viscous flow field about a cone-cylinder-flare body was calculated and compared to existing experimental data. Numerical predictions of the cone boundary layer and the flow field shock wave structure agreed with corresponding measurements. A separation was calculated at the cylinder-flare junction in six iterations; however, the size of the vortex did not correspond to the measured size. It was estimated that fifty iterations would be required to properly define the vortex. Conclusions of the study are that the iteration technique is of limited value for plane two-dimensional and axisymmetric flows, but of great value for three-dimensional flows.

NOMENCLATURE

a	Radius of the cylindrical cross-section
c	Local sound speed
C	Chapman-Rubesin constant
D	Diameter of cylindrical portion of cone-cylinder-flare body
E	Specific internal energy
f	Similarity parameter for the cone boundary layer
j	Index of mesh points in radial direction
J	Jacobian of the transformation and/or maximum number of mesh points in the radial direction
L	Reference length
m	Mass of a thermodynamic and/or momentum zone
M	Mach number
Mr	Radial momentum
Mz	Axial momentum
n	Distance normal to a surface
P	Pressure
Q	Artificial viscosity function
r	Radial coordinate
R	Reynolds number
s	Distance along a surface
S	Coordinate velocity in the radial direction
S _c	Safety factor for Δt_c
S _d	Safety factor for Δt_d
T	Temperature
t	Time

Δt	Timestep
Δt_c	Sound-speed controlled timestep
Δt_d	Viscous-diffusion-controlled timestep
U_e	Velocity component at outer edge of boundary layer
U	Radial velocity component
U_∞	Freestream velocity
\bar{U}	Local particle speed ($\bar{U} = \sqrt{U^2 + W^2}$)
W	Axial component of velocity
x	Cartesian coordinate of abscissa in cross-sectional plane of calculation
y	Cartesian coordinate of ordinate in cross-sectional plane of calculation
z	Axial coordinate
α	Freestream angle of attack with respect to the body axis
ψ	Stream function
μ	Viscosity
ν	Kinematic viscosity ($\nu = \frac{\mu}{\rho}$)
ρ	Density
ξ	Generalized radial coordinate
τ_{zr}	Shear stress
τ	Generalized time coordinate
σ_{rr}	Normal stress component in the radial direction
$\sigma_{\theta\theta}$	Normal stress component in the azimuthal direction
σ_{zz}	Normal stress component in the axial direction
w	Velocity difference $W - U_\infty$
$(\)_\infty$	Freestream condition
$(\)_e$	Property at outer edge of boundary layer

$(\)_r$	Reference condition for viscosity-temperature law
$(\)_p$	Property associated with flow on a flat plate
$(\)^n$	Property evaluated at t^n
$(\)^{n-1}$	Property evaluated at t^{n-1}
$(\)^{n-\frac{1}{2}}$	Property evaluated at $t^{n-\frac{1}{2}}$
$(\)^*$	Non-dimensional property

SECTION 1

INTRODUCTION

The purpose of this research effort is to develop a numerical method for computing steady, three-dimensional, viscous, compressible flow fields about aerodynamic bodies. The primary emphasis of this work is for supersonic axisymmetric flow; however, the method should extend to three spatial dimensions and to the subsonic and transonic flight regimes as well. Axisymmetric supersonic flow was studied to facilitate development of the numerical method. The advantages of starting with axisymmetric flow are discussed later in this section.

In 1969, under NASA AMES sponsorship, a research effort was initiated to apply the AFTON time-dependent two-dimensional computer code¹ to solve steady problems in three spatial dimensions. The idea was based on the Equivalence Principle,^{2,3} which states that for slender bodies at hypersonic speeds, the three-dimensional steady equations of motion for inviscid flow reduce identically to unsteady equations in two spatial dimensions.

The Equivalence Principle was extended in an ad hoc manner to a viscous flow through a model which permits viscous cross-flow, together with inviscid axial flow. Figure 1 shows an ogive-cylinder body at angle of attack α with respect to the freestream flow direction. Leeward vortices are indicated in the figure. The axial coordinate z was made

proportional to a time-like variable t according to the relation

$$z = U_\infty \cos \alpha t \quad (1)$$

The two-dimensional Navier-Stokes equations were then solved in cross-sectional planes normal to the system's axis. These cross-sectional planes were moved at freestream speed, U_∞ , from the leading edge to the trailing base of the body. The cross-sectional flow at each time, t , corresponded to steady flow at the z -coordinate given by Equation (1). It is noted that the leeward vortices of Figure 1 have axes almost parallel to the z -axis; therefore, the cross-sectional planes contain the vortices and the vortex calculation should be under the scope of the method.

Although all axial effects were neglected, this numerical procedure did calculate leeward vortices and produced other flow field results which were generally in accord with experiments. Numerical calculations were made and compared with experimental results for an ogive-cylinder and an airplane fuselage. Flow conditions were $M_\infty = 1.98$, $R_\infty = 4.68 \times 10^6$ /ft and $\alpha = 10^\circ$ for the ogive-cylinder and $M_\infty = 2.5$, $R_\infty = 9.1 \times 10^6$ /ft and $\alpha = 15^\circ$ for the fuselage configuration. Numerical-experimental comparisons were made of static pressure distributions on the body surface and contour plots of pitot pressure, total pressure, Mach number, and flow inclination at various cross-sectional planes normal to the system's axis. Maximum deviations of numerical surface pressures from corresponding experimental values were no more than 6 percent of free-stream dynamic pressure for both problems. Calculated pitot pressure contours were generally in accord with measured

contours on the windward side of the body. However, some differences were noted. Boundary layer separation and body vortex positions differed from experimental locations on the ogive-cylinder, and the shock induced by the fuselage canopy was predicted at a slightly different location. These differences were considered attributable to neglect of axial viscous effects, exclusion of turbulence phenomena, and the approximations introduced by the Equivalence Principle in describing the inviscid axial flow. Further details are presented in Reference 4.

In this research effort, axial effects are incorporated into the AFTON numerical procedure and a numerical solution to the full Navier-Stokes equations is generated by iteration. The steady-axisymmetric equations of motion are solved using a radial one-dimensional time-dependent computer code. Computational economy gained by one-dimensional calculation enabled the required experimentation with the finite difference technique to take place; hence, development of the complicated iteration method was made practical. The axisymmetric iteration method is applied to calculate the axisymmetric flow field about a cone-cylinder-flare body immersed in a supersonic airstream.

A discussion of the numerical method is presented in Section 2, results of the cone-cylinder-flare calculations are presented in Section 3, and the conclusions reached in this research effort are presented in Section 4.

SECTION 2

THE NUMERICAL METHOD

This section presents a general description of the iterative technique for solving the axisymmetric flow equations, formulation of the integral equations of motion for axisymmetric flow, and formulation of the finite difference approximations to them.

2.1 General Description of the Iteration Technique for Axisymmetric Flow

Rather than apply the Equivalence Principle in the ad hoc manner discussed in Section 1.0, it was decided to solve the full Navier-Stokes equations for axisymmetric flow by iteration. The calculational procedure would be similar to that described in Section 1.0, except that the axial convective and axial viscous terms dropped in the Equivalence Principle formulation will be evaluated from numerical data of a previous iterate. Consider the axially symmetric body shown in Figure 2. The steady-state axisymmetric flow field will be made analogous to time-dependent one-dimensional flow in a plane containing an expanding cylinder. The cross-sectional plane of unsteady analogy moves downstream with free-stream velocity and the outline of the moving boundary is given by the trace of the original shape in the cross-sectional plane; the moving boundary has the velocity V_n indicated in Figure 2. At station z (see Figure 2) the steady-state flow field in this plane is analogous to the flow field about the expanding cylinder (of radius a) at the time, $t = z/U_\infty$. Due to axial symmetry the time-dependent flow in each cross-sectional plane is radial. To make the analogy valid for a viscous fluid, no-slip flow

is imposed at the expanding cross-section. Far from the body free-stream conditions are imposed (i.e., $E = E_\infty$, $\rho = \rho_\infty$, $U = 0$, $W = V_\infty$).

The procedure for obtaining the first viscous iterate takes place in two steps. First, the inviscid solution or zeroth iterate is obtained. The flow field for the zeroth iterate is developed by dropping the viscous terms and axial convective terms from the equations of motion and applying the hypersonic Equivalence Principle^{2,3} directly. The first viscous iteration is obtained from the zeroth iterate by marching in z from the leading edge to the trailing base of the body and integrating the continuity, radial momentum, axial momentum and internal energy relations in a very special way. Axial convective and axial viscous terms are treated as source terms in the integration process and evaluated from numerical data from the zeroth iterate; linear interpolation in the inviscid field is used to evaluate the axial convective and axial viscous terms. All other terms are evaluated directly. In this way the mass, radial momentum, axial momentum, and internal energy are calculated throughout the axisymmetric flow field. After marching from the leading edge to the trailing base of the body, the first viscous iterate is obtained.

The second viscous iterate is obtained by going back to the leading edge and recalculating the flow field by marching to the base of the body. Calculation of the second iterate requires evaluation of the axial convective and axial viscous terms from numerical data for the first iterate. The procedure is then repeated to determine successive iterations until convergence occurs.

The iteration technique is further explained through the equations of motion presented in the next section.

2.2 Formulation of the Finite Difference Equations for Axisymmetric Flow

In this section finite difference equations are formulated for mass conservation, momentum conservation, and an internal energy theorem*. For illustrative purposes the finite difference equation for mass conservation will be derived. Let us consider a fixed axisymmetric body immersed in an airstream with freestream speed U_∞ parallel to the axis of the body; the axial direction is denoted by z and the radial direction by r . The conservation of mass for time-independent motion in the Eulerian coordinates r, z is as follows:

$$\frac{\partial(\rho W)}{\partial z} + \frac{1}{r} \frac{\partial(\rho Ur)}{\partial r} = 0 \quad (2)$$

where U is the local radial velocity, W is the local axial velocity, and ρ is the local material density. We now transform Equation (2) to the unsteady (r, t) plane using the relations

$$z = U_\infty t, \quad \frac{\partial}{\partial z} = \frac{1}{U_\infty} \frac{\partial}{\partial t}, \quad W = w + U_\infty \quad (3)$$

The transformed continuity equation is as follows:

$$\frac{\partial(\rho r)}{\partial t} + \frac{\partial(\rho Ur)}{\partial r} = - \frac{1}{U_\infty} \frac{\partial}{\partial t} (\rho wr) \quad (4)$$

The left-hand side of Equation (4) represents the continuity equation for time-dependent one-dimensional radial flow. The right-hand side of Equation (4) represents a source term which accounts for the variation of the axial velocity W . This term must be considered known in the iteration process and will be evaluated from the flow field of the previous iterate in each successive iteration.

* The internal energy is defined as the difference between total and kinetic energies.

Equation (4) is formulated in the Eulerian coordinates (r, t) ; however, in the planar calculational process the trace of the body surface in the plane must distort with time. Hence, we are really interested in the continuity equation in a generalized coordinate system ξ, τ , where

$$t = \tau \quad (5)$$

$$r = f(\xi, \tau) \quad (6)$$

and $f(\xi, 0) = \xi$, while $f_{\xi, \tau=0} = \frac{\partial f}{\partial \xi} \Big|_{\tau=0} = 1$.

We now differentiate (5) with respect to t and r , respectively, with the results

$$\left. \begin{aligned} 1 &= \frac{\partial \tau}{\partial t} \\ 0 &= \frac{\partial \tau}{\partial r} \end{aligned} \right\} \quad (7)$$

Performing the same differentiation of Equation (6) yields

$$\frac{\partial \xi}{\partial t} = - \frac{f_\tau}{f_\xi} \quad (8)$$

$$\frac{\partial \xi}{\partial r} = \frac{1}{f_\xi} \quad (9)$$

Consider the function $G(\xi, t)$ whose derivatives are

$$\frac{\partial G}{\partial r} = G_\xi \frac{\partial \xi}{\partial r} + G_\tau \frac{\partial \tau}{\partial r} = G_\xi / f_\xi \quad (10)$$

$$\frac{\partial G}{\partial t} = G_\xi \frac{\partial \xi}{\partial t} + G_\tau \frac{\partial \tau}{\partial t} = -G_\xi \frac{f_\tau}{f_\xi} + G_\tau \quad (11)$$

where use of Equations (7) - (9) produced Equations (10) and (11). Based on Equations (10) and (11), the continuity Equation (4) transforms to the generalized coordinates (ξ, τ) as follows:

$$\begin{aligned} - \frac{\partial(\rho r)}{\partial \xi} S + f_\xi \frac{\partial(\rho r)}{\partial \tau} + \frac{\partial(\rho Ur)}{\partial \xi} \\ = - \frac{1}{U_\infty} \left\{ - \frac{\partial}{\partial \xi} (\rho wr) S + f_\xi \frac{\partial}{\partial \tau} (\rho wr) \right\} \quad (12) \end{aligned}$$

where the grid velocity S is defined as

$$S = \frac{\partial r}{\partial \tau} = f_\tau \quad (13)$$

Now the partial derivative $\frac{\partial S}{\partial \xi}$ can be expressed as

$$\frac{\partial S}{\partial \xi} = \frac{\partial}{\partial \tau} \left(\frac{\partial f}{\partial \xi} \right) = \frac{\partial f_\xi}{\partial \tau} \quad (14)$$

Based on Equation (14), the continuity equation becomes

$$\begin{aligned} \frac{\partial}{\partial \tau} (\rho r f_\xi) + \frac{\partial}{\partial \xi} \left[\rho r (U - S) \right] - \frac{1}{U_\infty} \frac{\partial}{\partial \xi} (\rho wr S) \\ = - \frac{1}{U_\infty} \frac{\partial}{\partial \tau} \left[\rho wr f_\xi \right] \quad (15) \end{aligned}$$

Now integrating Equation (15) over ξ :

$$\begin{aligned} \frac{\partial}{\partial \tau} \int_{\xi_1}^{\xi_2} \rho r f_\xi d\xi + \rho r (U - S) \Big|_{\xi_1}^{\xi_2} - \frac{1}{U_\infty} \rho wr S \Big|_{\xi_1}^{\xi_2} \\ = - \frac{1}{U_\infty} \frac{\partial}{\partial \tau} \int_{\xi_1}^{\xi_2} \rho wr f_\xi d\xi \quad (16) \end{aligned}$$

where Liebnitz's rule is used to exchange differentiation and integration. The final step is to transform the ξ integrals of Equation (16) to r integrals. We know that

$$d\xi = J dr \quad (17)$$

where

$$= \begin{vmatrix} \frac{\partial \xi}{\partial r} & \frac{\partial \xi}{\partial t} \\ \frac{\partial r}{\partial \xi} & \frac{\partial t}{\partial \xi} \end{vmatrix} = \frac{1}{f_\xi}$$

Hence, the final integral continuity equation in generalized coordinates becomes

$$\begin{aligned} \frac{\partial}{\partial t} \int_{r_1}^{r_2} \rho r dr + \rho (U - S) r \Big|_{r_1}^{r_2} + \frac{1}{U_\infty} \rho r (U_\infty - W) S \Big|_{r_1}^{r_2} \\ = \frac{1}{U_\infty} \frac{\partial}{\partial t} \int_{r_1}^{r_2} \rho r (U_\infty - W) dr \end{aligned} \quad (18)$$

where Equation (3) is used to substitute for w in Equation (18).

The corresponding integral equations for radial and axial momentum, and specific internal energy are presented in Appendix A. It is noted that the heat conduction term is left out of the specific internal energy equation of Appendix A. The Stokesian stress-rate-of-strain relationship, the equation of state for a perfect gas, and a power law viscosity-temperature relationship* complete the system of equations.

We now derive the finite difference analog to continuity Equation (18). Consider a finite difference mesh along the

*The viscosity-temperature relationship is presented in Section 3.

r axis with the grid positions r_j , $j=1, \dots, J$. The finite difference mesh is illustrated in Figure 3. As seen from Figure 3 the region of calculation is divided into two sets of zones, one for the calculation of thermodynamic variables such as density, stress, internal energy, and the other for the calculation of momentum and velocity. Thermodynamic zones are indicated by solid lines and momentum zones by dashed lines. Thermodynamic properties are assumed homogeneous in solid zones and the momentum and velocity are assumed homogeneous in dashed zones. The AFTON 1 numerical procedure is employed to formulate the finite difference equations for this continuum structure⁵. Let the coordinate velocities S_j and particle velocities (U_j, W_j) be defined at the grid positions r_j and let the density $\rho_{j+\frac{1}{2}}$ be defined at the zone centers $r_{j+\frac{1}{2}} = \frac{1}{2}(r_j + r_{j+1})$. Based on the continuum structure of Figure 3, the finite difference approximation to Equation (18) for thermodynamic zone (r_j, r_{j+1}) is

$$\frac{m_{j+\frac{1}{2}}^n - m_{j+\frac{1}{2}}^{n-1}}{\Delta t} = \hat{M} + \hat{S} \quad (19)$$

where $m_{j+\frac{1}{2}}^n$ is the mass of zone (r_j, r_{j+1}) at time t^n , $m_{j+\frac{1}{2}}^{n-1}$ is the zone mass at time t^{n-1} , Δt the timestep and

$$\begin{aligned} \hat{M} = & - \left\{ \rho_{j+1}^{n-1} \left(U_{j+1}^{n-\frac{1}{2}} - S_{j+1}^{n-\frac{1}{2}} \right) r_{j+1}^{n-\frac{1}{2}} - \rho_j^{n-1} \left(U_j^{n-\frac{1}{2}} - S_j^{n-\frac{1}{2}} \right) r_j^{n-\frac{1}{2}} \right\}, \\ & - \frac{1}{U_\infty} \left\{ \rho_{s_{j+1}}^{n-1} \left(U_\infty - W_{j+1}^{n-\frac{1}{2}} \right) r_{j+1}^{n-\frac{1}{2}} S_{j+1}^{n-\frac{1}{2}} \right. \\ & \left. - \rho_{s_j}^{n-1} \left(U_\infty - W_j^{n-\frac{1}{2}} \right) r_j^{n-\frac{1}{2}} S_j^{n-\frac{1}{2}} \right\} \end{aligned} \quad (20)$$

$$\begin{aligned}
\hat{S} = & \frac{1}{U_\infty \Delta t} \left\{ \hat{\rho}_{j+\frac{1}{2}}^n \left[\left(U_\infty - \hat{W}_j^n \right) \left(\frac{r_{j+\frac{1}{2}}^n + r_j^n}{2} \right) \left(r_{j+\frac{1}{2}}^n - r_j^n \right) \right. \right. \\
& + \left(U_\infty - \hat{W}_{j+1}^n \right) \left(\frac{r_{j+1}^n + r_{j+\frac{1}{2}}^n}{2} \right) \left(r_{j+1}^n - r_{j+\frac{1}{2}}^n \right) \left. \right] \\
& - \hat{\rho}_{j+\frac{1}{2}}^{n-1} \left[\left(U_\infty - \hat{W}_j^{n-1} \right) \left(\frac{r_{j+\frac{1}{2}}^{n-1} + r_j^{n-1}}{2} \right) \left(r_{j+\frac{1}{2}}^{n-1} - r_j^{n-1} \right) \right. \\
& \left. \left. + \left(U_\infty - \hat{W}_{j+1}^{n-1} \right) \left(\frac{r_{j+1}^{n-1} + r_{j+\frac{1}{2}}^{n-1}}{2} \right) \left(r_{j+1}^{n-1} - r_{j+\frac{1}{2}}^{n-1} \right) \right] \right\} \quad (21)
\end{aligned}$$

The axial particle velocities \hat{W}_j^n , \hat{W}_j^{n-1} , \hat{W}_{j+1}^{n-1} and densities $\hat{\rho}_{j+\frac{1}{2}}^n$, $\hat{\rho}_{j+\frac{1}{2}}^{n-1}$ correspond to data from the previous iterate. The transport density $\hat{\rho}_{j+1}^{n-1}$ is defined as $\hat{\rho}_{j+1}^{n-1} = \hat{\rho}_{j+\frac{1}{2}}^{n-1}$ if the parameter $U_{j+1}^{n-\frac{1}{2}} - S_{j+1}^{n-\frac{1}{2}}$ is positive and $\hat{\rho}_{j+1}^{n-1} = \hat{\rho}_{j+\frac{3}{2}}^{n-1}$ if the parameter $U_{j+1}^{n-\frac{1}{2}} - S_{j+1}^{n-\frac{1}{2}}$ is negative. The transport density $\hat{\rho}_{s_{j+1}}^{n-1}$ is defined as $\hat{\rho}_{s_{j+1}}^{n-1} = \hat{\rho}_{j+\frac{1}{2}}^{n-1}$ if the parameter $S_{j+1}^{n-\frac{1}{2}}(U_\infty - \hat{W}_{j+1}^{n-\frac{1}{2}})$ is positive and $\hat{\rho}_{s_{j+1}}^{n-1} = \hat{\rho}_{j+\frac{3}{2}}^{n-1}$ if the parameter $S_{j+1}^{n-\frac{1}{2}}(U_\infty - \hat{W}_{j+1}^{n-\frac{1}{2}})$ is negative.

Considering the density to be homogeneous in zone (r_j, r_{j+1}) yields

$$\hat{\rho}_{j+\frac{1}{2}}^n = 2\hat{m}_{j+\frac{1}{2}}^n / (r_{j+1}^n + r_j^n) (r_{j+1}^n - r_j^n) \quad (22)$$

REPRODUCIBILITY OF THE
ORIGINAL PAGE IS POOR

2.3 Total Energy Conservation and Stability of the Finite Difference Equations

The finite difference equations presented in Section 2.2 and Appendix B are basically AFTON one-dimensional cylindrical equations⁵ with known source terms. As in the case of all AFTON finite difference relations, the equations of mass conservation, momentum conservation, the specific internal energy relation, and total energy conservation are redundant, i.e., any one of them can be deduced from the other three. More generally, any of the finite difference equations for mass conservation, total energy conservation, and the internal energy relation can be deduced from the other two taken together with the equation for momentum conservation. The only difference between the finite difference equations of Section 2.2 and Appendix B and the usual AFTON equations is that the source terms must be carried along in deriving the total energy equation from the continuity equation, axial momentum equation, radial momentum equation, and the internal energy relation.

Stability of the finite difference equations of Section 2.2 and Appendix B are governed by the usual sound speed and diffusion criteria; the source terms are known functions and therefore do not affect stability. The timestep for the calculation is governed by the smaller of the timesteps based on a sound speed criterion and a diffusion criterion.⁶

$$\Delta t_c = \frac{\Delta r_{\min}}{(U+c)S_c} \quad (23)$$

$$\Delta t_d = \frac{\Delta r_{\min}^2}{2 \nu S_d} \quad (24)$$

where Δt_c is the sound-speed controlled timestep, Δt_d the viscous diffusion controlled timestep, Δr_{\min} the minimum radial increment, \bar{U} the local particle speed ($U = \sqrt{U^2 + W^2}$), c the local sound speed, ν the kinematic viscosity, and S_c and S_d are the safety factors for sound speed controlled and diffusion controlled timesteps, respectively. The parameters S_c and S_d were set equal to two.

SECTION 3

RESULTS OF CALCULATIONS FOR A CONE-CYLINDER-FLARE BODY

In this section a general description of the problem is given, the inviscid solution to the problem is discussed, viscous solutions to the problem are presented, and the effects of separation on the iteration procedure are investigated.

3.1 General Description of Problem

After a literature survey and consultation with the Project Officer, supersonic flow over a cone-cylinder-flare body was selected as the problem for numerical evaluation. A sketch of the cone-cylinder-flare geometry is presented in Figure 4. The cylinder diameter is $D = 1.25$ inches and the cone and flare have 10 degree half-angles. The freestream Mach number is 4.54 and the freestream Reynolds number (based on cylinder diameter) is $R_\infty = 3.62 \times 10^5$. This case was experimentally studied by Kuehn⁷ at AMES Research Center. The quantities visually observed during the experiment were: (1) position of the separation point, and (2) the flow-field configuration, i.e., cone shock, flare shock wave-boundary layer interaction, and separated region at flare. The static pressure distribution was recorded along the cylinder-flare surface. These data will be compared with the numerical results.

The reasons behind the selection of the aforementioned case are outlined as follows:

- (A) The equivalence principle is readily applicable to the slender sharp-cone configuration.

- (B) Of the series of cone-cylinder-flare flows studied by Kuehn, the case selected had the highest Mach number, and therefore provides the simplest test of the applicability of the iteration technique.
- (C) The relatively short cylinder results in correspondingly few grid points in the streamwise direction, and therefore minimizes computer time requirements.
- (D) The Reynolds number is high enough so that separation indeed occurs.
- (E) The Reynolds number is low enough so that transition probably takes place at some distance from the model. At a similar Mach number, transition is observed at the flare at a Reynolds number of 5.35×10^5 , while there is no sign of transition at a Reynolds number of 4.97×10^5 . Hence the entire boundary layer for the selected case is laminar.
- (F) The flare angle of 10° is large enough to give an observable separated zone.
- (G) The boundary-layer thickness at the location where separation is about to occur is approximately $0.042"$, or $1/30$ of the cylinder diameter. Hence, a reasonably detailed picture of the flow field can be expected from the computation.
- (H) At the station referenced in item (G), the static pressure is about 90 percent of the free-stream pressure; there is no region in the flow field where the density is substantially less than the ambient density, hence, it will not be necessary to employ unusually high mesh point densities for the calculation.

The medium considered was air with a polytropic γ = 1.4.

uent γ of 1.4 and with the following viscosity-temperature law

$$\mu = \mu_r \left(\frac{E}{E_r} \right)^{.98} \quad (25)$$

where $\mu_r = 3.33 \times 10^5$ dyne-sec/cm², and $E_r = 3.405 \times 10^8$ dyne-cm/gram.

3.2. Mesh Boundary Conditions, and Initial Conditions Used

The finite difference mesh for the cone-cylinder-flare problem was composed of 50 points and automatically distorted as the cylindrical trace of the body distorted in the cross-sectional plane. The finite difference mesh in the vicinity of the body at axial station $z = 8.29$ cm. is shown in Figure 5. The wedge-like radial region of calculation has an upstream boundary at the radius $r = 1.46$ cm. and has its lateral boundary at $r = 7$ cm. The zones are closely spaced in the vicinity of the body and coarsely spaced near the lateral boundary. About six zones exist in the boundary layer near the cone-cylinder junction; this is further discussed in Section 3.4.2.

Boundary conditions along the radial wedge-like region of calculation were as follows:

- (1) No-slip flow on the upstream boundary.
- (2) Freestream conditions on the lateral boundary, i.e.,
 $\rho = \rho_\infty, E = E_\infty, U = 0, W = U_\infty$.
- (3) Axial symmetry on the side-walls of the wedge.

The calculation did not commence from the leading edge of the cone, but started at a distance of $z_0 = .567$ cm. down-

stream of the leading edge. At the cross-sectional plane corresponding to this downstream distance, impulsive initial conditions were imposed, i.e., freestream flow about the cone surface ($\rho = \rho_\infty$, $E = E_\infty$, $U = 0$, $W = W_\infty$) and no-slip flow at the surface ($U = 0$, $W = 0$).

3.3 Zeroth Iterate: The Inviscid Flow Field

The zeroth iterate, in an iterative computational procedure to solve for the viscous, compressible flow about a cone-cylinder-flare configuration, is described in this section. The zeroth iterate consisted of the steady, inviscid flow field about this configuration subject to the assumptions of the Hayes Equivalence Principle.^{2,3} To solve this inviscid cone-cylinder-flare problem a hydrodynamic computer code, written in a generalized coordinate system, was developed for transient one-dimensional cylindrical flow, and the transient solution was converted to the steady inviscid flow field about the cone-cylinder-flare configuration via the Hayes Equivalence Principle.^{2,3} This computer code is designated "AFTON 1". The AFTON 1 computer code was developed by programming the finite difference equations of Reference 5 to solve for flow fields on a finite difference mesh whose velocities can be prescribed in an arbitrary manner. The finite difference equations for the Lagrangian coordinate system were first programmed and debugged. While running the cone-cylinder-flare problem, it was found that the Lagrangian formulation produced zones so thin that the calculational timestep was reduced to a level which increased computer time requirements above the practical range. Hence, the generalized coordinate system was introduced and zones

were prescribed to be thicker as the problem progressed. Based on the AFTON 1 computer code and the finite difference mesh of 50 points, the machine time required to solve the inviscid cone-cylinder-flare problem was 5 minutes on a Univac 1108 computer. To attain this solution, whose results are discussed in the next two paragraphs, 2500 cycles (i.e., time-steps) of calculation were required.

Results of the numerical calculations are compared to the experimental data of Kuehn⁷ and with the known inviscid solution for the cone portion of the body.⁸ The numerical cone shock angle and cone surface pressure ratio (P/P_∞) were 16.2° and 2.065, respectively, while the corresponding theoretical inviscid values are 16.5° and 2.08. Further details of the comparison of the numerical results with experiment are presented below.

The numerical results for the inviscid cone-cylinder-flare body are compared to the experimental data of Kuehn in Figure 6. The body configuration is indicated in the figure (cross-hatched line) as well as the numerical cone shock locus, flare shock locus, and surface pressure distribution. The experimental surface pressure distribution, cone shock locus, separation shock locus, and flare (or reattachment) shock locus are also indicated. It is seen from Figure 6 that the numerical shock angle is slightly smaller than the measured shock angle; this is in accord with physical reality because the boundary layer displacement effect is not present in the numerical inviscid calculations. The experimental pressure distribution is close to the numerical one upstream of the flare-corner interaction region and approaches the numerical pressures downstream of this interaction region; this result is physically reasonable since viscous effects are only important in the neighborhood of the flare-corner. Finally,

the experimental flare (or reattachment) shock locus nearly coincides with the corresponding numerical shock locus. This result is at first somewhat disturbing, since the flow upstream of the flare-corner has passed through the separation shock, and thus has a lower incident Mach number than the corresponding inviscid flow. Hence, the experimental flare shock angle should be greater than the inviscid angle. However, due to separation the flow immediately downstream of the separation shock is flowing at a nonzero angle. Therefore the flare angle relative to this stream of fluid is less than the geometrical flare angle of 10^0 and this will produce a flare shock angle smaller than the inviscid one. The two counter-balancing factors can result in an experimental flare shock angle almost equal to the inviscid prediction.

3.4 First, Second and Third Iterates: The Viscous Flow Field

The finite difference equations for steady viscous, compressible, axisymmetric flow, which were formulated in Section 2.2, were incorporated into the AFTON 1 computer code. The revised AFTON 1 computer code was then capable of solving the viscous cone-cylinder-flare problem of Section 3. The solution was obtained through an iteration process based on the Equivalence Principle solution as the zeroth iterate. The revised AFTON 1 code was then checked out by performing hand calculations with the finite difference equations of motion and comparing them with computer output for the cone-cylinder-flare problem. In addition to the hand calculations, the conservation properties of the AFTON 1 finite difference equations were checked. After seven cycles, i.e., timesteps, of computation, a zone-by-zone summation of the total energy (internal plus kinetic) of material in the region of

calculation was identical (within seven places) to the total energy that results from the conservation of total energy theorem for the entire region of calculation.

Based on the AFTON 1 computer code and the finite difference mesh of 50 points, the time required to solve for the first viscous iterate to the cone-cylinder-flare problem was 40 minutes on the Univac 1108 computer. To obtain this solution, whose results are discussed in the remainder of this section, approximately 7000 cycles (i.e., timesteps) were required. This represents a considerable increase in computational time with respect to the zeroth iterate, which required 5 minutes and only 2500 cycles. However, a time-dependent solution to the unsteady Navier-Stokes equations for axisymmetric flow would require about 12 hours on a Univac 1108 computer, so that the inherent economy of the procedure is clearly indicated through the first two iterates.

3.4.1 Flow Field and Pressure Distribution

A velocity vector plot of the cone-cylinder-flare flow field after three viscous iterations is shown in Figure 7. Each column of vectors represents the solution in one cross-sectional plane. The vectors in each column emanate from the mesh points along the radial line in that cross-sectional plane; their magnitudes are proportional to the local particle speeds. Curve 1 denotes the calculated cone shock locus and Curve 2 denotes the calculated flare shock locus. Shock transitions were calculated with an artificial viscosity, i.e., Q-function, proportional to the square of the velocity divergence.⁶ However, the Q-function was limited only to the neighborhood of the shock transitions. A thin boundary layer is seen as a dark line near the body surface; the calculated

boundary layer thickness was approximately 2% of the cylinder diameter near the cone-cylinder junction.

The numerical results of the zeroth and first iterates are compared to the experimental data of Kuehn in Figure 8. The body configuration is indicated in the figure as well as numerical cone shock loci, flare shock loci, and surface pressure distributions for both the zeroth and first iterates. The experimental surface pressure distribution, cone shock locus, separation shock locus, and flare (or reattachment) shock locus are also indicated. The experimental cone shock angle is 17.6° ; by comparison the first iterate cone shock angle is 17.0° , while the cone shock angle of the zeroth iterate is 16.5° . This represents a 3.4% error in cone shock angle for the first iterate and an 8.5% error for the second iterate. The flare shock angle has remained almost constant in going from the zeroth to the first iterate.

The surface pressure distributions of the zeroth and first iterates are almost identical and clearly do not match the data in the region of separation at the cylinder-flare junction because the boundary layer computed in the first iterate did not separate at the cylinder-flare junction. Subsequent iterations would be required to determine the subsonic recirculation region associated with separation.

3.4.2 The Cone-Boundary Layer for Infinite Prandtl Number

As was mentioned in Section 2.2, heat conduction was left out of the internal energy relation solved in this numerical investigation. Hence, the numerical solutions generated correspond to infinite Prandtl number. Unfortunately, to the best of our knowledge, there are no available boundary

layer theory predictions to compare to for flow along a cone at infinite Prandtl number. However, the Chapman-Rubesin flat plate boundary layer velocity profile,⁹ corrected for axial symmetry by the Mangler transformation,¹⁰ is independent of the energy equation if plotted as a function of the similarity parameter

$$f = \frac{\psi}{\sqrt{\mu_e \rho_e U_e C s}} \quad (26)$$

where ψ is the stream function for axially symmetric flow, U_e is the velocity at the boundary layer edge, ρ_e is the density at the boundary layer edge, μ_e is the viscosity at the boundary layer edge, C is the Chapman-Rubesin constant, and s is distance along the cone surface. The Chapman-Rubesin boundary layer velocity profile for flow along a cone is discussed further in Appendix C.

The numerical results for the cone boundary layer velocity profile, corresponding to the first and second iterates are compared to the Chapman-Rubesin profile in Figure 9. The numerical data correspond to an axial station z of 8.73 cm. and a Chapman-Rubesin constant C of .88875. The velocity profile for the first iterate has an inflection point and has a maximum deviation from the theoretical profile of no more than 17%. However, the boundary layer profile for the second iterate coincides with the Chapman-Rubesin prediction. Hence, after two viscous iterations the cone boundary layer has been calculated correctly.

3.5 Separation at the Cylinder-Flare Junction

One of the principal objectives of this research effort is to investigate the feasibility of predicting flow separation through the iteration procedure. Experimentally,⁷ it has been shown that the flow separates at the cylinder-flare junction and an axisymmetric vortex forms there. In this section the numerical results of five viscous iterations are examined in the neighborhood of the cylinder-flare junction to determine the extent to which the method can predict separation.

Development of the flow field in the vicinity of the cylinder-flare junction is presented in the form of velocity vector plots in Figures 10, 11 and 12. Figure 10 presents the flow field after three viscous iterations, Figure 11 after four viscous iterations, and finally Figure 12 after five viscous iterations. The + symbols in each figure represent the body surface. It is seen from Figure 10 that after three iterations the flow is only slightly perturbed at the cylinder-flare junction, and definitely is not separated. Figure 11, after four viscous iterations, shows the flow to be near separating but not quite separated. Finally, Figure 12, after five viscous iterations, shows that separation has been initiated.

Based on the above results, it seems clear that the calculation of flow separation through successive iterations is possible but may not be practical. It is anticipated that approximately fifty iterations may be required to completely define the vortex at the cylinder-flare junction.

The cone-cylinder-flare problem could not be continued past the fifth viscous iteration. During computation of the

sixth viscous iterate, large oscillations were recorded along the cone surface, which finally produced a negative mass--i.e., a "numerical singular point." It is believed that discretization error, defined as the difference between the exact value of a property of the continuum and the value determined from a discrete approximation to the continuum, is the primary cause of termination of the iteration procedure. Past experience has shown that discretization errors produce small spatial and timewise oscillations in the numerical flow field. Flow field oscillations in the cone-cylinder-flare problem built up fluctuations in the source terms of the equations of motion in each successive iteration. The fluctuating source terms eventually caused the failure on the cone surface during the sixth viscous iteration. It is believed that the iteration procedure could be continued if the discretization oscillations were removed from the flow field.

SECTION 4

CONCLUSIONS

Based on the results of Section 3, two principal conclusions emerge regarding the iteration technique for solving the full Navier-Stokes equations.

- (1) The iteration technique is capable of correctly predicting details of the flow field which have little or no upstream influence, such as a boundary layer or a shock wave.
- (2) Although theoretically possible, it is impractical to calculate separations which lie outside the plane of calculation through the iteration procedure. The cylinder-flare junction vortex has its axis parallel to the cross-sectional planes of calculation; hence, it lies outside these planes.

The above conclusions indicate that the application of one-dimensional time-dependent methods to solve for steady plane two-dimensional and/or axially symmetric flow fields are of limited value. These one-dimensional methods will be capable of predicting only those flow phenomena with little or no upstream influence, i.e., a boundary layer or a shock wave. Vortices, in plane two-dimensional and axisymmetric flows will always lie outside the planes of calculation; therefore, they are beyond the scope of one-dimensional methods.

Conclusions (1) and (2) also clearly indicate that the application of two-dimensional time-dependent methods to solve for steady flow fields in three spatial dimensions is of great value. In a three dimensional flow problem, one can always

select a two-dimensional plane of calculation which will be nearly normal to the axes of vortices in the flow field. There are two excellent examples of three-dimensional flows which are definitely under the scope of this iteration technique. The first is a body at angle-of-attack and the second is a three-dimensional wing.

The body at angle-of-attack problem is a simple one for the iteration technique. Experimentally determined axial velocity profiles¹¹ on the lee side of a 10° half-angle cone, at 12° angle of attack, freestream Mach number 7.87, and Reynolds number 8.51×10^5 (referred to the cone base diameter), and boundary-layer-like. The recirculation region occurs in cross-sectional planes normal to the body's axis. Application of the iteration technique in cross-sectional planes will surely be successful.

The three-dimensional sweptback wing problem is more difficult for the iteration technique, but definitely feasible. This problem generally has two types of vortices. In a plane normal to the wing span, i.e., a cross-sectional plane, the principal vortex will exist. Furthermore, due to the presence of the wing tip, a secondary vortex could exist in a plane normal to the free-stream flow direction. To solve the wing problem the integration must be done in two different directions in the iteration procedure. First, two iterations are required in cross-sectional planes of the wing. These iterations will define the principal vortex. Secondly, a third iteration is required in planes normal to the free-stream flow direction to determine the secondary (tip) vortex and other wing tip effects. It is believed that in three iterations, as described above, the flow field about a three-dimensional swept-back wing can be calculated.

APPENDIX A
INTEGRAL EQUATIONS FOR AXISYMMETRIC FLOW

In this appendix the integral equations for momentum conservation and the internal energy theorem are presented for axisymmetric flow. These relations are first presented in differential form for an Eulerian coordinate system and then shown in their integral form for a generalized coordinate system.

Consider a fixed axisymmetric body immersed in an air-stream with freestream speed U_∞ parallel to the axis of the body; the axial direction is denoted by z and the radial direction by r . The radial momentum equation, axial momentum equation, and internal energy relation in Eulerian cylindrical coordinates r and z are as follows:

Radial Momentum

$$\frac{\partial}{\partial z} (\rho WU) + \frac{1}{r} \frac{\partial}{\partial r} (\rho U^2 r) = \frac{1}{r} \left[\frac{\partial (r\sigma_{rr})}{\partial r} + \frac{\partial (r\tau_{zr})}{\partial z} \right] - \frac{\sigma_{\theta\theta}}{r} \quad (A1)$$

Axial Momentum

$$\frac{\partial}{\partial z} (\rho WW) + \frac{1}{r} \frac{\partial}{\partial r} (\rho r WU) = \frac{1}{r} \left[\frac{\partial (r\tau_{zr})}{\partial r} + \frac{\partial (r\sigma_{zz})}{\partial z} \right] \quad (A2)$$

Internal Energy Relation

$$\frac{\partial}{\partial z} (\rho WE) + \frac{1}{r} \frac{\partial}{\partial r} (\rho UrE) = \quad (\text{cont'd})$$

$$= \sigma_{zz} \frac{\partial W}{\partial z} + \sigma_{rr} \frac{\partial U}{\partial r} + \tau_{zr} \left(\frac{\partial U}{\partial z} + \frac{\partial W}{\partial r} \right) + \frac{U}{r} \sigma_{\theta\theta} \quad (A3)$$

where E is the specific internal energy, U is the local radial velocity, W is the local axial velocity, and σ is the local material density. The parameters σ_{rr} , τ_{zr} , $\sigma_{\theta\theta}$ and σ_{zz} are the stress components in the radial, tangential, azimuthal, and axial directions, respectively. Equations (A1), (A2), and (A3) are then transformed to the unsteady (r, t) plane using the relations

$$z = U_{\infty} t, \frac{\partial}{\partial z} = \frac{1}{U_{\infty}} \frac{\partial}{\partial t}, W = w + U_{\infty} \quad (A4)$$

The transformed equations are formulated in the Eulerian coordinates (r, t) ; however, in the planar calculational process the trace of the body surface in the plane distorts with time. Hence, we are really interested in the equations of motion in a generalized coordinate system ξ , τ , where

$$t = \tau \quad (A5)$$

$$r = f(\xi, \tau) \quad (A6)$$

and $f(\xi, 0) = \xi$, while $f_{\xi} \Big|_{\tau=0} = \left(\frac{\partial f}{\partial \xi} \right)_{\tau=0} = 1$. Proceeding through the same derivation as outlined in Section 2.2 for the continuity equation yields the remaining integral relations.

Radial Momentum

$$\begin{aligned}
 & \frac{\partial}{\partial \tau} \int_{r_1}^{r_2} \rho U r dr + \left[\rho (U - S) r U \right]_{r_1}^{r_2} + \left[\rho U (U_{\infty} - W) r \frac{S}{U_{\infty}} \right]_{r_1}^{r_2} \\
 &= \left[r \sigma_{rr} \right]_{r_1}^{r_2} - \int_{r_1}^{r_2} \sigma_{\theta\theta} dr - \left[\frac{\tau_{zr} r S}{U_{\infty}} \right]_{r_1}^{r_2} \\
 &+ \frac{1}{U_{\infty}} \frac{\partial}{\partial \tau} \int_{r_1}^{r_2} \tau_{zr} r dr + \frac{1}{U_{\infty}} \frac{\partial}{\partial \tau} \int_{r_1}^{r_2} \rho U (U_{\infty} - W) r dr \quad (A7)
 \end{aligned}$$

Axial Momentum

$$\begin{aligned}
 & \frac{\partial}{\partial \tau} \int_{r_1}^{r_2} \rho W r dr + \left[\rho r W (U - S) \right]_{r_1}^{r_2} + \left[\rho W (U_{\infty} - W) r \frac{S}{U_{\infty}} \right]_{r_1}^{r_2} \\
 &= \left[r \tau_{zr} \right]_{r_1}^{r_2} - \left[\frac{\sigma_{zz} r S}{U_{\infty}} \right]_{r_1}^{r_2} + \frac{1}{U_{\infty}} \frac{\partial}{\partial \tau} \int_{r_1}^{r_2} \sigma_{zz} r dr \\
 &+ \frac{1}{U_{\infty}} \frac{\partial}{\partial \tau} \int_{r_1}^{r_2} \rho r W (U_{\infty} - W) dr \quad (A8)
 \end{aligned}$$

Internal Energy Relation

$$\begin{aligned}
 & \frac{\partial}{\partial \tau} \int_{r_1}^{r_2} \rho E r dr + \left[\rho r E (U - S) \right]_{r_1}^{r_2} + \left[\rho r E (U_{\infty} - W) \frac{S}{U_{\infty}} \right]_{r_1}^{r_2} = \\
 & \quad \text{(cont'd)}
 \end{aligned}$$

$$\begin{aligned}
&= \int_{U_1}^{U_2} \sigma_{rr} r dU \pm \int_{r_1}^{r_2} U \sigma_{\theta\theta} dr + \int_{W_1}^{W_2} r \tau_{zr} dW - \left[\frac{\sigma_{zz}}{U_\infty} WrS \right]_{r_1}^{r_2} \\
&\quad - \left[\frac{\tau_{zr}}{U_\infty} UrS \right]_{r_1}^{r_2} + \frac{\sigma_{zz}}{U_\infty} \frac{\partial}{\partial r} \int_{r_1}^{r_2} r W dr + \frac{\tau_{zr}}{U_\infty} \frac{\partial}{\partial r} \int_{r_1}^{r_2} r U dr
\end{aligned} \tag{A9}$$

where the bracket $\left[\dots \right]_{r_1}^{r_2}$ implies that the term contained is evaluated at the limits r_1 and r_2 . Equations (A7), (A8), and (A9) in conjunction with Equation (18) represent the four conservation relations solved numerically for the dependent variables ρ , E , U and W .

APPENDIX B

FINITE DIFFERENCE EQUATIONS FOR AXISYMMETRIC FLOW

The finite difference analogs to integral momentum Equations (A5) and (A6) and the integral internal energy Equation (A7) are presented in this appendix. Consider the finite difference mesh along the r axis with the grid positions r_j , $j=1, \dots, J$. The finite difference mesh is illustrated in Figure 3. Let the coordinate velocities S_j and particle velocities (U_j, W_j) be defined at the grid positions r_j and let the density $\rho_{j+\frac{1}{2}}$ and energy $E_{j+\frac{1}{2}}$ be defined at the zone centers $r_{j+\frac{1}{2}} = \frac{1}{2}(r_j + r_{j+1})$. Based on the continuum structure of Figure 3, the finite difference approximations to the momentum equations (Equations (A7) and (A8)) are written for the momentum zone $(r_{j-\frac{1}{2}}, r_{j+\frac{1}{2}})$, while the finite difference approximation to the internal energy relation (Equation A9) is written for the thermodynamic zone (r_j, r_{j+1}) . These relations are as follows:

Radial Momentum

$$\frac{M_{r_j}^n - M_{r_j}^{n-1}}{\Delta t} = \hat{M}_r + \hat{S}_r + \hat{F}_r + \hat{G}_r \quad (B1)$$

where $M_{r_j}^n$ is the radial momentum of momentum zone $(r_{j-\frac{1}{2}}, r_{j+\frac{1}{2}})$ at the time t^n , $(M_{r_j}^{n-1})$ is the radial momentum of momentum zone $(r_{j-\frac{1}{2}}, r_{j+\frac{1}{2}})$ at time t^{n-1} , Δt is the timestep and \hat{M}_r , \hat{S}_r , \hat{F}_r and \hat{G}_r are defined as follows:

$$\begin{aligned}
\hat{M}_r &= - \left\{ \mu_{j+\frac{1}{2}}^{n-\frac{1}{2}} \left(\frac{U_{j+1}^{n-\frac{1}{2}} + U_j^{n-\frac{1}{2}}}{2} \right) - \mu_{j-\frac{1}{2}}^{n-\frac{1}{2}} \left(\frac{U_j^{n-\frac{1}{2}} + U_{j-1}^{n-\frac{1}{2}}}{2} \right) \right\} \\
&\quad - \frac{1}{U_\infty} \left\{ \mu_{s_{j+\frac{1}{2}}}^{n-\frac{1}{2}} \left(\frac{U_{j+1}^{n-\frac{1}{2}} + U_j^{n-\frac{1}{2}}}{2} \right) - \mu_{s_{j-\frac{1}{2}}}^{n-\frac{1}{2}} \left(\frac{U_j^{n-\frac{1}{2}} + U_{j-1}^{n-\frac{1}{2}}}{2} \right) \right\}
\end{aligned} \tag{B2}$$

where

$$\begin{aligned}
\mu_{j+\frac{1}{2}}^{n-\frac{1}{2}} &= \frac{1}{2} \left[\rho_{j+1}^{n-1} (U_{j+\frac{1}{2}}^{n-\frac{1}{2}} - S_{j+1}^{n-\frac{1}{2}}) r_{r+1}^{n-\frac{1}{2}} + \rho_j^{n-1} (U_j^{n-\frac{1}{2}} - S_j^{n-\frac{1}{2}}) r_j^{n-\frac{1}{2}} \right] \\
\mu_{s_{j+\frac{1}{2}}}^{n-\frac{1}{2}} &= \frac{1}{2} \left[\rho_{s_{j+1}}^{n-1} (U_\infty - W_{j+1}^{n-\frac{1}{2}}) r_{j+1}^{n-\frac{1}{2}} S_{j+1}^{n-\frac{1}{2}} + \right. \\
&\quad \left. \rho_{s_j}^{n-1} (U_\infty - W_j^{n-\frac{1}{2}}) r_j^{n-\frac{1}{2}} S_j^{n-\frac{1}{2}} \right]
\end{aligned}$$

and the transport densities ρ_{j+1}^{n-1} , ρ_j^{n-1} , $\rho_{s_{j+1}}^{n-1}$, and $\rho_{s_j}^{n-1}$ are defined in Section 2.2.

$$\begin{aligned}
\hat{S}_r &= \frac{1}{U_\infty \Delta t} \left\{ (U_\infty - \tilde{W}_j^n) \tilde{U}_j^n \left[\tilde{\rho}_{j+\frac{1}{2}}^n \left(\frac{r_{j+\frac{1}{2}}^n + r_j^n}{2} \right) (r_{j+\frac{1}{2}}^n - r_j^n) \right. \right. \\
&\quad \left. \left. + \tilde{\rho}_{j-\frac{1}{2}}^n \left(\frac{r_j^n + r_{j-\frac{1}{2}}^n}{2} \right) (r_j^n - r_{j-\frac{1}{2}}^n) \right] \right. \\
&\quad \left. - (U_\infty - \tilde{W}_j^{n-1}) \tilde{U}_j^{n-1} \left[\tilde{\rho}_{j+\frac{1}{2}}^{n-1} \left(\frac{r_{j+\frac{1}{2}}^{n-1} + r_j^{n-1}}{2} \right) (r_{j+\frac{1}{2}}^{n-1} - r_j^{n-1}) \right. \right. \\
&\quad \left. \left. + \tilde{\rho}_{j-\frac{1}{2}}^{n-1} \left(\frac{r_j^{n-1} + r_{j-\frac{1}{2}}^{n-1}}{2} \right) (r_j^{n-1} - r_{j-\frac{1}{2}}^{n-1}) \right] \right\}
\end{aligned} \tag{B3}$$

The radial and axial particle velocities $\tilde{U}_j^n, \tilde{U}_j^{n-1}, \tilde{W}_j^n, \tilde{W}_j^{n-1}$ and the densities $\tilde{\rho}_{j+\frac{1}{2}}^n, \tilde{\rho}_{j+\frac{1}{2}}^{n-1}, \tilde{\rho}_{j-\frac{1}{2}}^n, \tilde{\rho}_{j-\frac{1}{2}}^{n-1}$ correspond to data from the previous iterate.

$$\begin{aligned} \hat{F}_r = & r_{j+\frac{1}{2}}^{n-\frac{1}{2}} \sigma_{rr}^{n-\frac{1}{2}} - r_{j-\frac{1}{2}}^{n-\frac{1}{2}} \sigma_{rr}^{n-\frac{1}{2}} - \left[\sigma_{\theta\theta}^{n-\frac{1}{2}} (r_{j+\frac{1}{2}}^{n-\frac{1}{2}} - r_{j-\frac{1}{2}}^{n-\frac{1}{2}}) \right. \\ & \left. + \sigma_{\theta\theta}^{n-\frac{1}{2}} (r_j^{n-\frac{1}{2}} - r_{j-\frac{1}{2}}^{n-\frac{1}{2}}) \right] \end{aligned} \quad (B4)$$

where $\sigma_{rr}^{n-\frac{1}{2}}$ corresponds to the radial normal stress in zone (r_j, r_{j+1}) at the time $t^{n-\frac{1}{2}}$ and $\sigma_{\theta\theta}^{n-\frac{1}{2}}$ corresponds to the azimuthal stress in zone (r_j, r_{j+1}) at time $t^{n-\frac{1}{2}}$. To conform to the stability criteria of the AFTON 1. differencing scheme, the stress $\sigma_{rr}^{n-\frac{1}{2}}$ is evaluated as the arithmetic average between the stresses $\sigma_{rr}^n_{j+\frac{1}{2}}$ and $\sigma_{rr}^{n-1}_{j+\frac{1}{2}}$. The stress $\sigma_{rr}^n_{j+\frac{1}{2}}$ is evaluated from the sum of a pressure term at t^n and a viscous term at $t^{n-\frac{1}{2}}$; velocity data from the previous iterate are used to determine derivatives of z in the $\sigma_{rr}^n_{j+\frac{1}{2}}$ formula.

$$\begin{aligned} \hat{G}_r = & \frac{1}{U_\infty \Delta t} \left\{ \left[\tau_{zr}^n_{j+\frac{1}{2}} \left(\frac{r_{j+\frac{1}{2}}^n + r_j^n}{2} \right) (r_{j+\frac{1}{2}}^n - r_j^n) + \tau_{zr}^{n-1}_{j-\frac{1}{2}} \left(\frac{r_j^n + r_{j-\frac{1}{2}}^n}{2} \right) (r_j^n - r_{j-\frac{1}{2}}^n) \right] \right. \\ & - \left[\tau_{zr}^{n-1}_{j+\frac{1}{2}} (r_{j+\frac{1}{2}}^{n-1} + r_j^{n-1}) (r_{j+\frac{1}{2}}^{n-1} - r_j^{n-1}) + \tau_{zr}^{n-1}_{j-\frac{1}{2}} \left(\frac{r_j^{n-1} + r_{j-\frac{1}{2}}^{n-1}}{2} \right) (r_j^{n-1} - r_{j-\frac{1}{2}}^{n-1}) \right] \\ & \left. - \frac{1}{U_\infty} \left\{ \tau_{zr}^{n-\frac{1}{2}}_{j+\frac{1}{2}} r_{j+\frac{1}{2}}^{n-\frac{1}{2}} \left(\frac{S_{j+\frac{1}{2}}^{n-\frac{1}{2}} + S_{j+\frac{1}{2}}^{n-\frac{1}{2}}}{2} \right) - \tau_{zr}^{n-\frac{1}{2}}_{j-\frac{1}{2}} r_{j-\frac{1}{2}}^{n-\frac{1}{2}} \left(\frac{S_j^{n-\frac{1}{2}} + S_{j-\frac{1}{2}}^{n-\frac{1}{2}}}{2} \right) \right\} \right\} \end{aligned} \quad (B5)$$

where $\tau_{zr}^{n,j+\frac{1}{2}}$ is the shear stress of zone r_j, r_{j+1} evaluated at time $t^{n-\frac{1}{2}}$ and $\tau_{zr}^{n-1,j+\frac{1}{2}}$ to the shear stress of zone (r_j, r_{j+1}) at time $t^{n-\frac{1}{2}}$. Data from the previous iterate are used to evaluate derivatives of z in the formulae for $\tau_{zr}^{n,j+\frac{1}{2}}$ and $\tau_{zr}^{n-1,j+\frac{1}{2}}$. The stress $\tau_{zr}^{n-\frac{1}{2}}$ is taken as the arithmetic average of $\tau_{zr}^{n,j+\frac{1}{2}}$ and $\tau_{zr}^{n-1,j+\frac{1}{2}}$.

Axial Momentum

$$\frac{M_{z,j}^n - M_{z,j}^{n-1}}{\Delta t} = \hat{M}_z + \hat{S}_z + \hat{F}_z + \hat{G}_z \quad (B6)$$

where $M_{z,j}^n$ is the axial momentum of momentum zone $(r_{j-\frac{1}{2}}, r_{j+\frac{1}{2}})$ at time t^{n-1} , and \hat{M}_z , \hat{S}_z , \hat{F}_z , and \hat{G}_z are defined as follows:

$$\begin{aligned} \hat{M}_z &= - \left\{ \mu_{j+\frac{1}{2}}^{n-\frac{1}{2}} \left(\frac{W_{j+1}^{n-\frac{1}{2}} + W_j^{n-\frac{1}{2}}}{2} \right) - \mu_{j-\frac{1}{2}}^{n-\frac{1}{2}} \left(\frac{W_j^{n-\frac{1}{2}} + W_{j-1}^{n-\frac{1}{2}}}{2} \right) \right\} \\ &\quad - \frac{1}{U_\infty} \left\{ \mu_{s,j+\frac{1}{2}}^{n-\frac{1}{2}} \left(\frac{W_{j+1}^{n-\frac{1}{2}} + W_j^{n-\frac{1}{2}}}{2} \right) - \mu_{s,j-\frac{1}{2}}^{n-\frac{1}{2}} \left(\frac{W_j^{n-\frac{1}{2}} + W_{j-1}^{n-\frac{1}{2}}}{2} \right) \right\} \quad (B7) \end{aligned}$$

$$\begin{aligned} \hat{S}_z &= \frac{1}{U_\infty \Delta t} \left\{ (U_\infty - \tilde{W}_j^n) \tilde{W}_j^n \left[\tilde{\rho}_{j+\frac{1}{2}}^n \left(\frac{r_{j+\frac{1}{2}}^n + r_j^n}{2} \right) (r_{j+\frac{1}{2}}^n - r_j^n) \right. \right. \\ &\quad \left. \left. + \tilde{\rho}_{j-\frac{1}{2}}^n \left(\frac{r_j^n + r_{j-\frac{1}{2}}^n}{2} \right) (r_j^n - r_{j-\frac{1}{2}}^n) \right] \right. \\ &\quad \left. - (U_\infty - \tilde{W}_j^{n-1}) \tilde{W}_j^{n-1} \left[\tilde{\rho}_{j+\frac{1}{2}}^{n-1} \left(\frac{r_{j+\frac{1}{2}}^{n-1} + r_j^{n-1}}{2} \right) (r_{j+\frac{1}{2}}^{n-1} - r_j^{n-1}) \right. \right. \\ &\quad \left. \left. + \tilde{\rho}_{j-\frac{1}{2}}^{n-1} \left(\frac{r_j^{n-1} + r_{j-\frac{1}{2}}^{n-1}}{2} \right) (r_j^{n-1} - r_{j-\frac{1}{2}}^{n-1}) \right] \right\} \quad (B8) \end{aligned}$$

$$\begin{aligned}
\hat{G}_z = \frac{1}{U_\infty \Delta t} & \left\{ \left[\sigma_{zz,j+\frac{1}{2}}^n \left(\frac{r_{j+\frac{1}{2}}^n + r_j^n}{2} \right) (r_{j+\frac{1}{2}}^n - r_j^n) + \sigma_{zz,j-\frac{1}{2}}^n \left(\frac{r_{j+\frac{1}{2}}^n + r_{j-\frac{1}{2}}^n}{2} \right) (r_j^n - r_{j-\frac{1}{2}}^n) \right] \right. \\
& - \left[\sigma_{zz,j+\frac{1}{2}}^{n-1} \left(r_{j+\frac{1}{2}}^{n-1} + r_j^{n-1} \right) (r_{j+\frac{1}{2}}^{n-1} - r_j^{n-1}) + \sigma_{zz,j-\frac{1}{2}}^{n-1} \left(\frac{r_{j+\frac{1}{2}}^{n-1} + r_{j-\frac{1}{2}}^{n-1}}{2} \right) (r_j^{n-1} - r_{j-\frac{1}{2}}^{n-1}) \right] \\
& \left. - \frac{1}{U_\infty} \left\{ \sigma_{zz,j+\frac{1}{2}}^{n-\frac{1}{2}} r_{j+\frac{1}{2}}^{n-\frac{1}{2}} \left(\frac{S_j^{n-\frac{1}{2}} + S_{j+\frac{1}{2}}^{n-\frac{1}{2}}}{2} \right) - \sigma_{zz,j-\frac{1}{2}}^{n-\frac{1}{2}} r_{j-\frac{1}{2}}^{n-\frac{1}{2}} \left(\frac{S_j^{n-\frac{1}{2}} + S_{j-\frac{1}{2}}^{n-\frac{1}{2}}}{2} \right) \right\} \right] \quad (B9)
\end{aligned}$$

where $\sigma_{zz,j+\frac{1}{2}}^n$ is the axial normal stress of zone (r_j, r_{j+1}) at time t^n and $\sigma_{zz,j+\frac{1}{2}}^{n-1}$ is the axial normal stress of zone (r_j, r_{j+1}) at time t^{n-1} . The stress $\sigma_{zz,j+\frac{1}{2}}^n$ is evaluated from the sum of a pressure term at t^n and a viscous term at $t^{n-\frac{1}{2}}$; velocity data from the previous iterate are used to determine derivatives of z in the $\sigma_{zz,j+\frac{1}{2}}^n$ formula. The stress $\sigma_{zz,j+\frac{1}{2}}^{n-\frac{1}{2}}$ is evaluated from the arithmetic average of $\sigma_{zz,j+\frac{1}{2}}^n$ and $\sigma_{zz,j+\frac{1}{2}}^{n-1}$.

Internal Energy Relation

$$\frac{m_{j+\frac{1}{2}}^n E_{j+\frac{1}{2}}^n - m_{j+\frac{1}{2}}^{n-1} E_{j+\frac{1}{2}}^{n-1}}{\Delta t} = \hat{M}_E + \hat{S}_E + \hat{W}_E + \hat{G}_{EZ} + \hat{G}_{ER} \quad (B10)$$

where $E_{j+\frac{1}{2}}^n$ is the specific internal energy of thermodynamic zone (r_j, r_{j+1}) at time t^n , $E_{j+\frac{1}{2}}^{n-1}$ is the specific internal energy of thermodynamic zone (r_j, r_{j+1}) at time t^{n-1} , $m_{j+\frac{1}{2}}^n$ is the mass of thermodynamic zone (r_j, r_{j+1}) at time t^n , $m_{j+\frac{1}{2}}^{n-1}$ is the mass of thermodynamic zone (r_j, r_{j+1}) at time t^{n-1} , and \hat{M}_E , \hat{S}_E , \hat{W}_E , \hat{G}_{EZ} and \hat{G}_{ER} are defined as follows:

REPRODUCIBILITY OF THE
ORIGINAL PAGE IS POOR

$$\begin{aligned}
\hat{M}_E &= - \left\{ \rho_{j+1}^{n-1} (U_{j+1}^{n-\frac{1}{2}} - S_{j+1}^{n-\frac{1}{2}}) r_{j+1}^{n-\frac{1}{2}} E_{j+1}^{n-1} - \rho_j^{n-1} (U_j^{n-\frac{1}{2}} - S_j^{n-\frac{1}{2}}) r_j^{n-\frac{1}{2}} E_j^{n-1} \right\} \\
&\quad - \frac{1}{U_\infty} \left\{ \rho_{s_{j+1}}^{n-1} (U_\infty - W_{j+1}^{n-\frac{1}{2}}) r_{j+1}^{n-\frac{1}{2}} S_{j+1}^{n-\frac{1}{2}} E_{s_{j+1}}^{n-1} \right. \\
&\quad \left. - \rho_{s_{j+1}}^{n-1} (U_\infty - W_j^{n-\frac{1}{2}}) r_j^{n-\frac{1}{2}} S_j^{n-\frac{1}{2}} E_{s_j}^{n-1} \right\} \quad (B11)
\end{aligned}$$

where the transport energies E_{j+1}^{n-1} and $E_{s_{j+1}}^{n-1}$ are defined in a manner analogous to the definition of the transport densities of Section 2.2.

$$\begin{aligned}
\hat{S}_E &= \frac{1}{U_\infty \Delta t} \left\{ \rho_{j+\frac{1}{2}}^n \tilde{E}_{j+\frac{1}{2}}^n \left[(U_\infty - \tilde{W}_j^n) \left(\frac{r_{j+\frac{1}{2}}^n + r_j^n}{2} \right) (r_{j+\frac{1}{2}}^n - r_j^n) \right. \right. \\
&\quad + (U_\infty - \tilde{W}_{j+1}^n) \left(\frac{r_{j+1}^n + r_{j+\frac{1}{2}}^n}{2} \right) (r_{j+1}^n - r_{j+\frac{1}{2}}^n) \\
&\quad \left. \left. - \rho_{j+\frac{1}{2}}^{n-1} \tilde{E}_{j+\frac{1}{2}}^{n-1} \left[(U_\infty - \tilde{W}_n^{n-1}) (r_{j+\frac{1}{2}}^{n-1} + r_j^{n-1}) - (r_{j+\frac{1}{2}}^{n-1} - r_j^{n-1}) \right. \right. \right. \\
&\quad \left. \left. + (U_\infty - \tilde{W}_{j+1}^{n-1}) \left(\frac{r_{j+1}^{n-1} + r_{j+\frac{1}{2}}^{n-1}}{2} \right) (r_{j+1}^{n-1} - r_{j+\frac{1}{2}}^{n-1}) \right] \right\} \quad (B12)
\end{aligned}$$

The specific internal energies $\tilde{E}_{j+\frac{1}{2}}^n$, $\tilde{E}_{j+\frac{1}{2}}^{n-1}$ correspond to data from the previous iterate.

$$\begin{aligned}
\hat{W}_E &= \sigma_{rr}^{n-\frac{1}{2}} r_{j+\frac{1}{2}}^{n-\frac{1}{2}} (U_{j+1}^{n-\frac{1}{2}} - U_j^{n-\frac{1}{2}}) + \left(\frac{U_{j+1} + U_j}{2} \right) \sigma_{\theta\theta}^{n-\frac{1}{2}} (r_{j+1}^{n-\frac{1}{2}} - r_j^{n-\frac{1}{2}}) \\
&+ \tau_{zr}^{n-\frac{1}{2}} \left(\frac{r_{j+1} + r_j}{2} \right) (W_{j+1}^{n-\frac{1}{2}} - W_j^{n-\frac{1}{2}}) \quad (B13)
\end{aligned}$$

$$\begin{aligned}
\hat{G}_{EZ} &= \frac{\sigma_{zz}^{n-\frac{1}{2}}}{U_\infty \Delta t} \left\{ \left[\tilde{W}_{j+1}^n \left(\frac{r_{j+1}^n + r_{j+\frac{1}{2}}^n}{2} \right) (r_{j+1}^n - r_{j+\frac{1}{2}}^n) + \tilde{W}_j^n \left(\frac{r_{j+\frac{1}{2}}^n + r_j^n}{2} \right) (r_{j+\frac{1}{2}}^n - r_j^n) \right] \right. \\
&- \left. \left[\tilde{W}_{j+1}^{n-1} \left(\frac{r_{j+1}^{n-1} + r_{j+\frac{1}{2}}^{n-1}}{2} \right) (r_{j+1}^{n-1} - r_{j+\frac{1}{2}}^{n-1}) + \tilde{W}_j^{n-1} \left(\frac{r_{j+\frac{1}{2}}^{n-1} + r_j^{n-1}}{2} \right) (r_{j+\frac{1}{2}}^{n-1} - r_j^{n-1}) \right] \right\} \\
&- \frac{\sigma_{zz}^{n-\frac{1}{2}}}{U_\infty} \left\{ W_{j+1}^{n-\frac{1}{2}} r_{j+1}^{n-\frac{1}{2}} s_{j+1}^{n-\frac{1}{2}} - W_j^{n-\frac{1}{2}} r_j^{n-\frac{1}{2}} s_j^{n-\frac{1}{2}} \right\} \quad (B14)
\end{aligned}$$

$$\begin{aligned}
\hat{G}_{Er} &= \frac{\tau_{zr}^{n-\frac{1}{2}}}{U_\infty \Delta t} \left\{ \left[\tilde{U}_{j+1}^n \left(\frac{r_{j+1}^n + r_{j+\frac{1}{2}}^n}{2} \right) (r_{j+1}^n - r_{j+\frac{1}{2}}^n) + \tilde{U}_j^n \left(\frac{r_{j+\frac{1}{2}}^n + r_j^n}{2} \right) (r_{j+\frac{1}{2}}^n - r_j^n) \right] \right. \\
&- \left. \left[\tilde{U}_{j+1}^{n-1} \left(\frac{r_{j+1}^{n-1} + r_{j+\frac{1}{2}}^{n-1}}{2} \right) (r_{j+1}^{n-1} - r_{j+\frac{1}{2}}^{n-1}) + \tilde{U}_j^{n-1} \left(\frac{r_{j+\frac{1}{2}}^{n-1} + r_j^{n-1}}{2} \right) (r_{j+\frac{1}{2}}^{n-1} - r_j^{n-1}) \right] \right\} \\
&- \frac{\tau_{zr}^{n-\frac{1}{2}}}{U_\infty} \left\{ \tilde{U}_{j+1}^{n-\frac{1}{2}} \tilde{r}_{j+1}^{n-\frac{1}{2}} \tilde{s}_{j+1}^{n-\frac{1}{2}} - \tilde{U}_j^{n-\frac{1}{2}} \tilde{r}_j^{n-\frac{1}{2}} \tilde{s}_j^{n-\frac{1}{2}} \right\} \quad (B15)
\end{aligned}$$

where the particle velocities \tilde{U}_{j+1}^n , \tilde{U}_{j+1}^{n-1} , \tilde{U}_j^n , \tilde{U}_j^{n-1} correspond to data from the previous iterate.

REPRODUCIBILITY OF THE
ORIGINAL PAGE IS POOR

APPENDIX C

CHAPMAN-RUBESIN BOUNDARY LAYER VELOCITY PROFILE ON A CONE

The Chapman-Rubesin flat plate boundary layer velocity profile,⁹ corrected for axial symmetry by the Mangler transformation,¹⁰ is independent of the energy equation if plotted as a function of the similarity parameter

$$f = \frac{\psi}{\sqrt{\frac{u_e \rho_e C U_s}{\mu_e} s}}$$
 (C1)

where ψ is the stream function for axially symmetric flow, U_e is the velocity at the boundary layer edge, ρ_e is the density at the boundary layer edge, μ_e is the viscosity at the boundary layer edge, C is the Chapman-Rubesin constant and s is distance along the cone surface. In this appendix the Chapman-Rubesin boundary layer velocity profile for a cone is derived. This derivation starts with a flat plate geometry and then the results are transformed to a cone.

The Chapman-Rubesin velocity profile for a flat plate is based on the principal assumption that the viscosity in the boundary layer is proportional to the temperature in the boundary layer. The following relation is assumed for the viscosity-temperature relationship:

$$\frac{\mu}{\mu_e} = C \left(\frac{T}{T_e} \right)$$
 (G2)

where μ is the local viscosity, T the local temperature and T_e the temperature at the boundary layer edge.

Chapman and Rubesin then introduce non-dimensional forms of velocity, temperature, stream function, density, and so on, as follows:

$$\left. \begin{aligned} U^* &= \frac{U}{U_e}, \quad T^* = \frac{T}{T_e}, \quad s_p^* = \frac{s_p}{L}, \quad \sigma^* = \frac{\sigma}{\sigma_e} \\ \mu_e^* &= \frac{\mu}{\mu_e}, \quad \psi_p^* = \frac{\psi_p}{\sqrt{\mu_e \sigma_e U_e L C}}, \quad n_p^* = \frac{n_p}{L} \end{aligned} \right\} \quad (C3)$$

where L is a characteristic distance, n is the distance normal to the surface and the subscript "p" denotes a property associated with the flat-plate flow. The absence of a subscript "p" denotes a property which is invariant to the geometry of the system, i.e., the same for a flat plate and a cone. In terms of the non-dimensional variables of Equations (C3), the boundary layer momentum equation becomes

$$\frac{\partial U^*}{\partial s_p^*} = \frac{\partial}{\partial \psi_p^*} (U^* \frac{\partial U^*}{\partial \psi_p^*}) \quad (C4)$$

where the usual independent variables of non-dimensional distance along the plate s_p^* and non-dimensional distance normal to the plate n_p^* have been replaced by the non-dimensional stream function ψ_p^* and non-dimensional distance along the plate s_p^* according to the von Mises transformation.¹² Equation (C4) does not have the temperature or density in it; hence, it is independent of the energy equation.

Partial differential equation (C4) is then reduced to a total differential equation through the similarity parameter

$$f_p = \frac{\psi_p^*}{\sqrt{s_p^*}} \quad (C5)$$

and the assumption that

$$U^* = U_p^*(f_p) \quad (C6)$$

Introduction of Equations (C5) and (C6) into Equation (C4) yields

$$- \frac{f_p}{2} \frac{dU^*}{df_p} = \frac{d}{df_p} (U^* \frac{dU^*}{df_p}) \quad (C7)$$

Let us now assume that f_p is a function of another dummy variable η and that the non-dimensional velocity profile is given by

$$u^* = f_p^*(\eta) \quad (C8)$$

Introduction of Equation (C8) into Equation (C7) yields the final differential equation

$$2f_p''' + f_p f_p'' = 0 \quad (C9)$$

Equation (C9) is identical to the Blasius flat plate equation for incompressible flow.¹³ Therefore, according to Equation (C6) and (C8), the Blasius solution for the non-dimensional velocity profile on a flat plate represents the compressible profile if plotted as a function of the Blasius stream function f_p .

It is now necessary to transform the known flat plate velocity profile to suit flow along a cone. For this purpose the Mangler transformation¹⁰ is used. The flat plate stream function f_p and distance along the plate s_p transform to corresponding cone properties according to the following relations:

$$\left. \begin{aligned} \psi &= \frac{\psi_p}{L} \\ s &= \frac{s_p^3}{3} \frac{\sin^2 \theta_c}{L^2} \end{aligned} \right\} \quad (C10)$$

where θ_c is the cone half-angle. The Blasius stream function f_p then transforms to the cone geometry as follows:

$$f = f_p \frac{s \sin \theta_c}{\sqrt{3}} \quad (C11)$$

where f is defined, given by Equation (C1). Hence, if the Blasius velocity profile is plotted as a function of f (given by Equation (C11)), the boundary-layer velocity profile for compressible flow on a cone results.

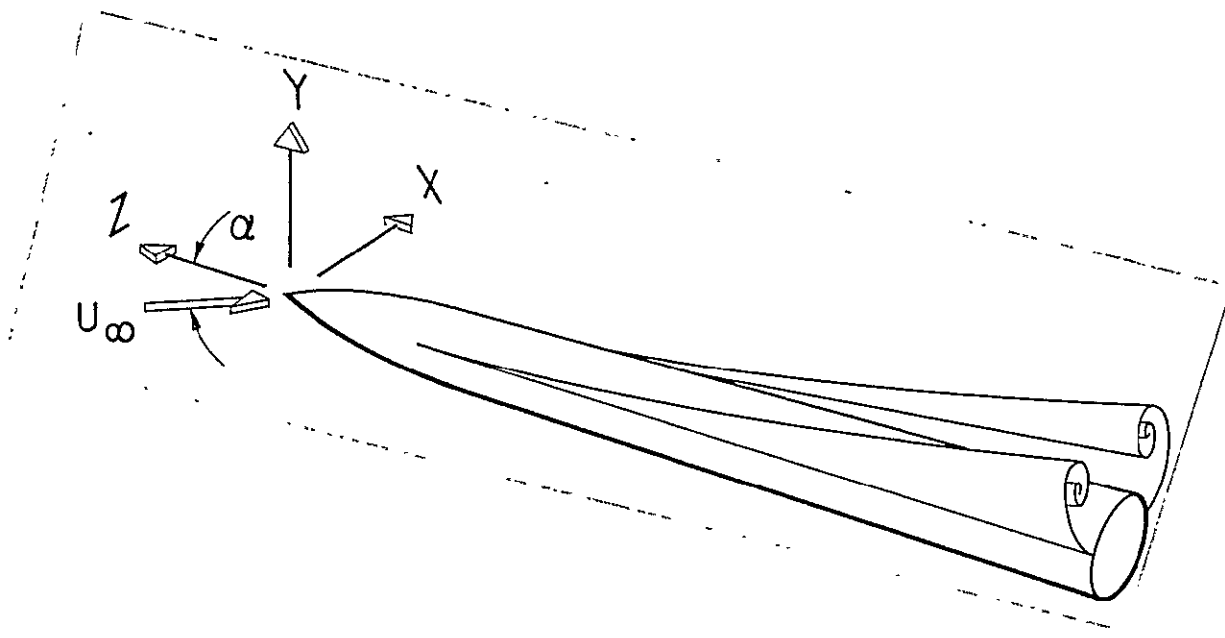


Figure 1. Flow Field About an Axisymmetric Body at Angle of Attack.

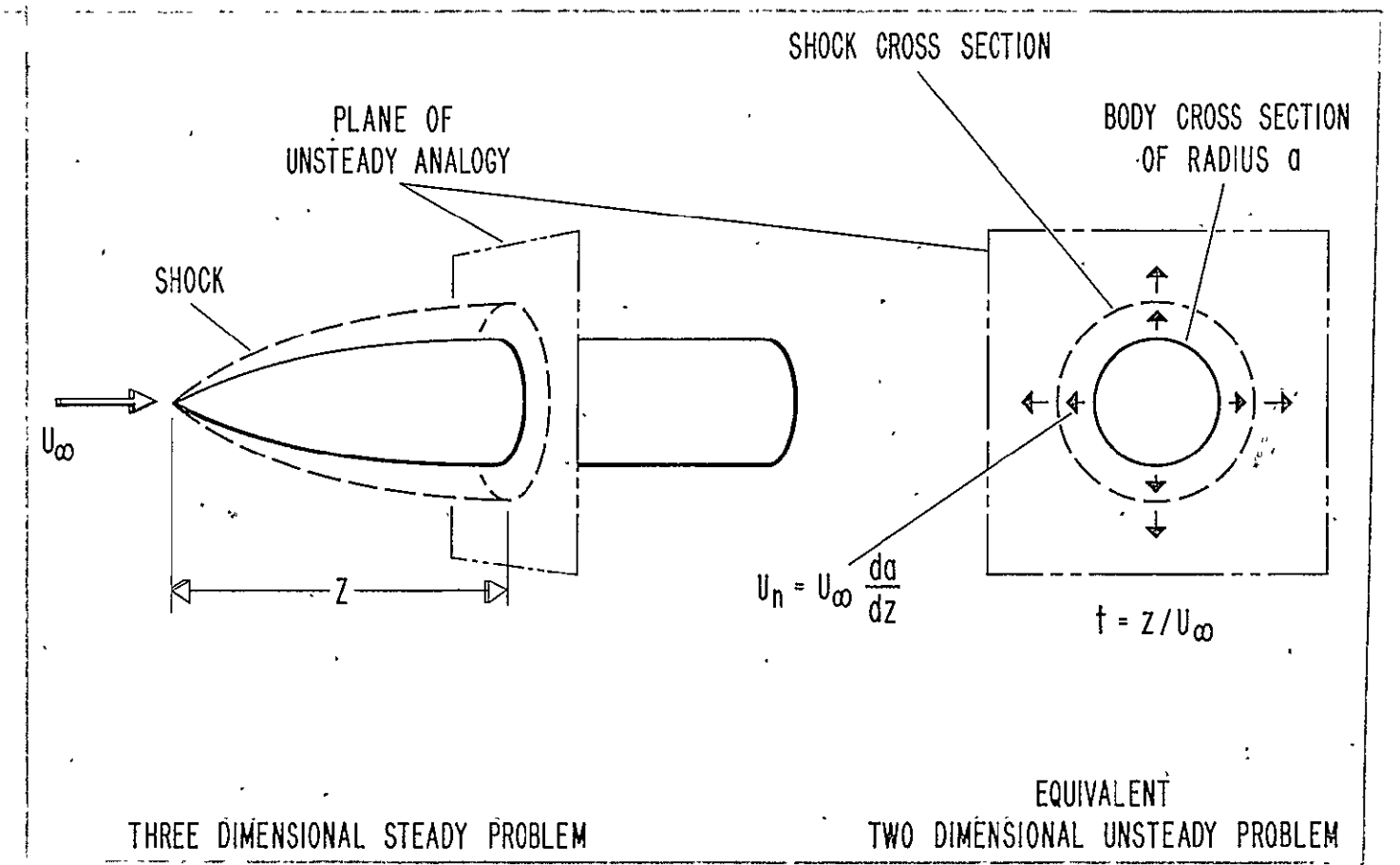


Figure 2. Application of the Iteration Technique to an Axisymmetric Body.

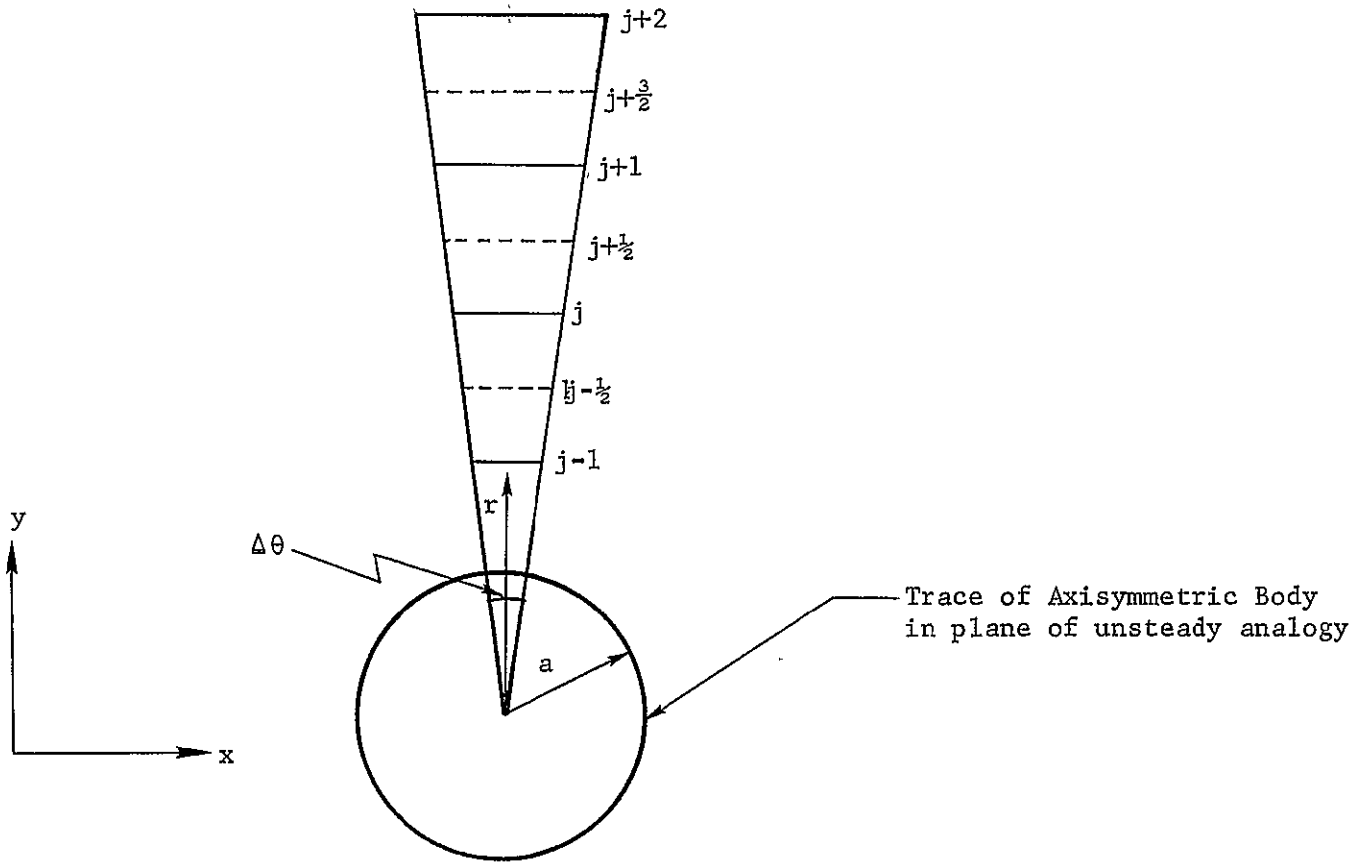
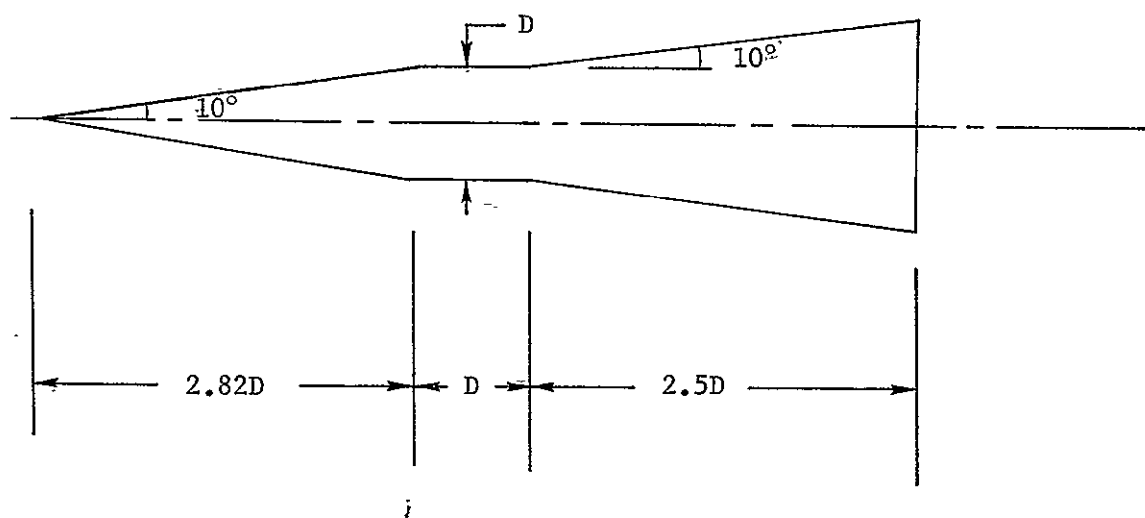


Figure 3. Schematic of Three Thermodynamic Zones and Two Momentum Zones for Radial One-Dimensional Time-Dependent Motion; solid lines indicate thermodynamic zones; dashed lines indicate momentum zones; a indicates cylinder radius.



$$D = 1.25 \text{ in}$$

Freestream Mach Number $M_\infty = 4.42$

Freestream Reynolds Number (based on cylinder diameter); $R_\infty = 3.62 \times 10^5$

Figure 4. Schematic of Cone-Cylinder-Flare Geometry Numerically Investigated.

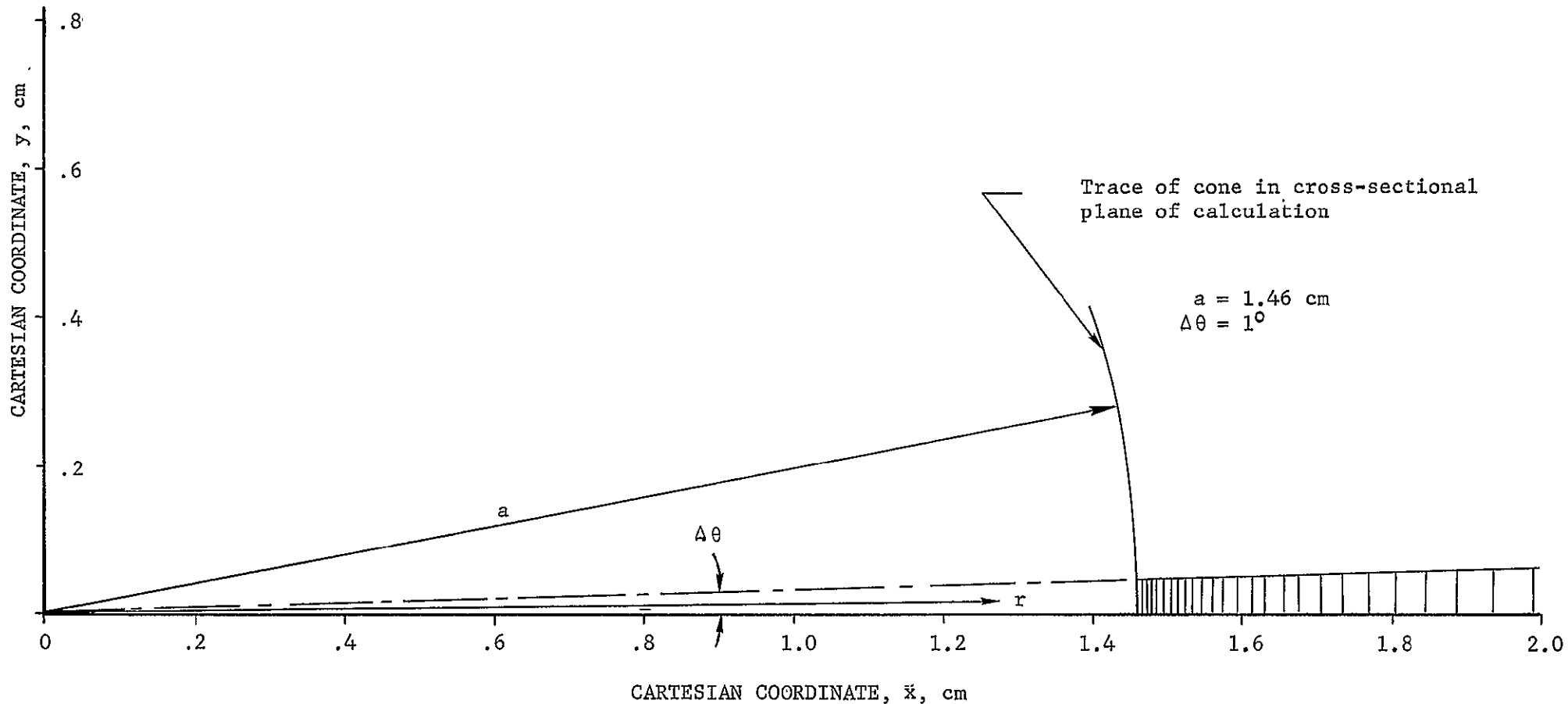


Figure 5. Finite Difference Mesh Along a Wedge-Like Radial Region of Calculation in the (\bar{x}, \bar{y}) Cross-section Plane at an Axial Station z of 8.29 cm; a denotes the radius of the trace of the body in the cross-sectional plane; $\Delta\theta$ corresponds to the azimuthal angle of the wedge-like radial region; the flow is symmetrical with respect to θ but varies in the radial direction.

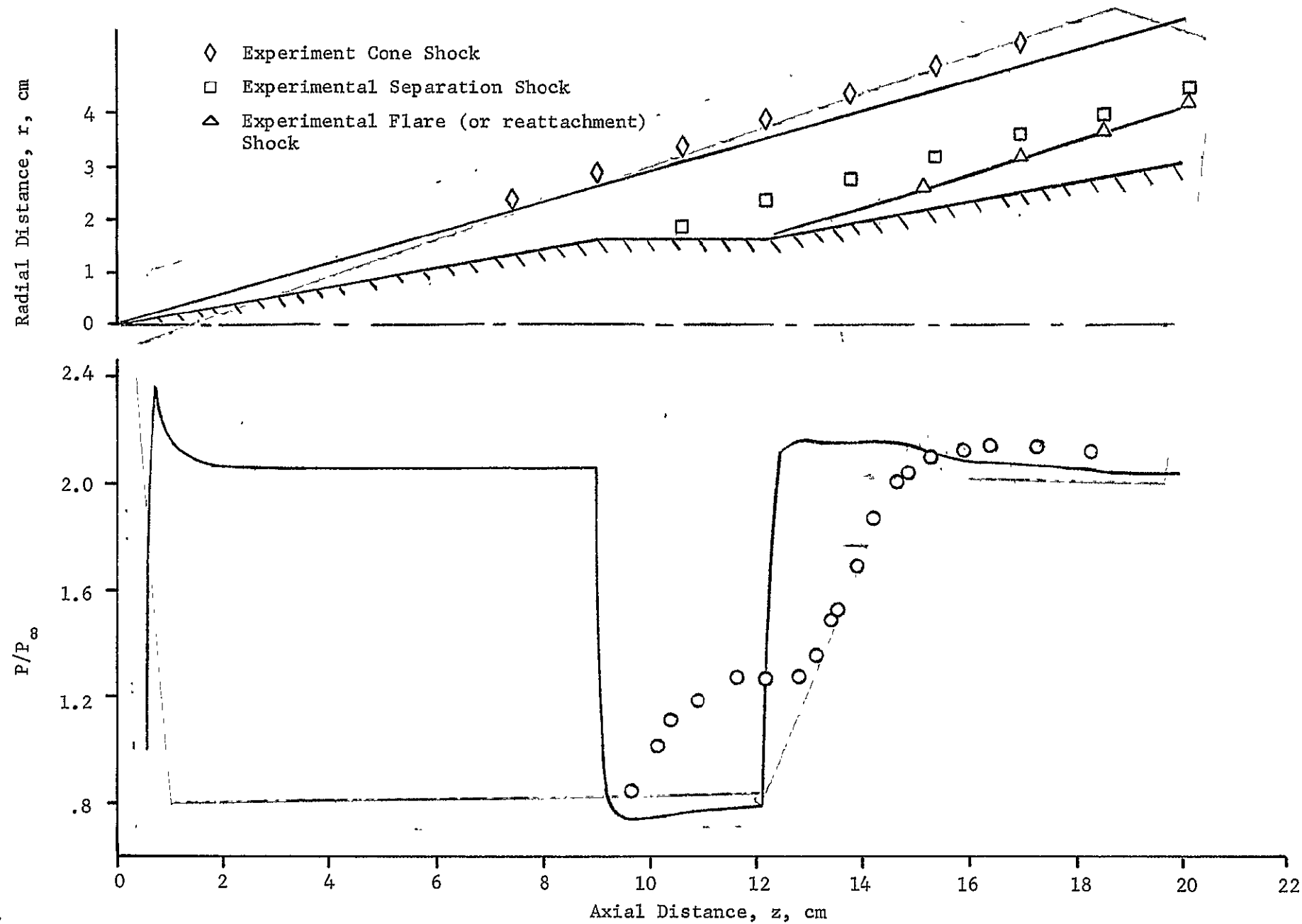
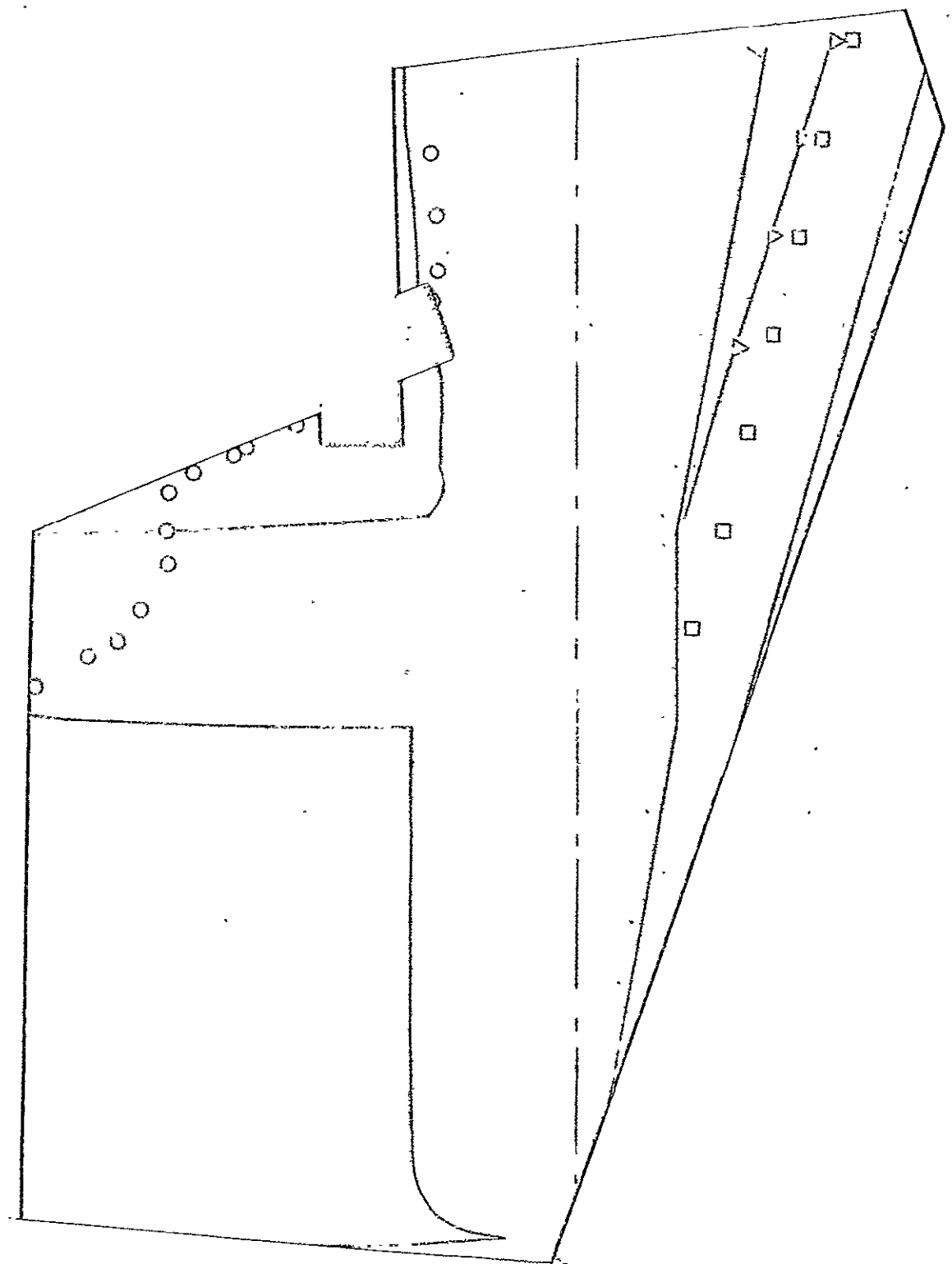


Figure 6. Comparison of Inviscid Numerical Results with Experimental Surface Pressure Distributions and Shock Loci; $M_\infty = 4.42$, $R_\infty = 1.14 \times 10^5$ per cm; solid lines indicate numerical results, cross-hatched line indicates body geometry, and symbols indicate data points.



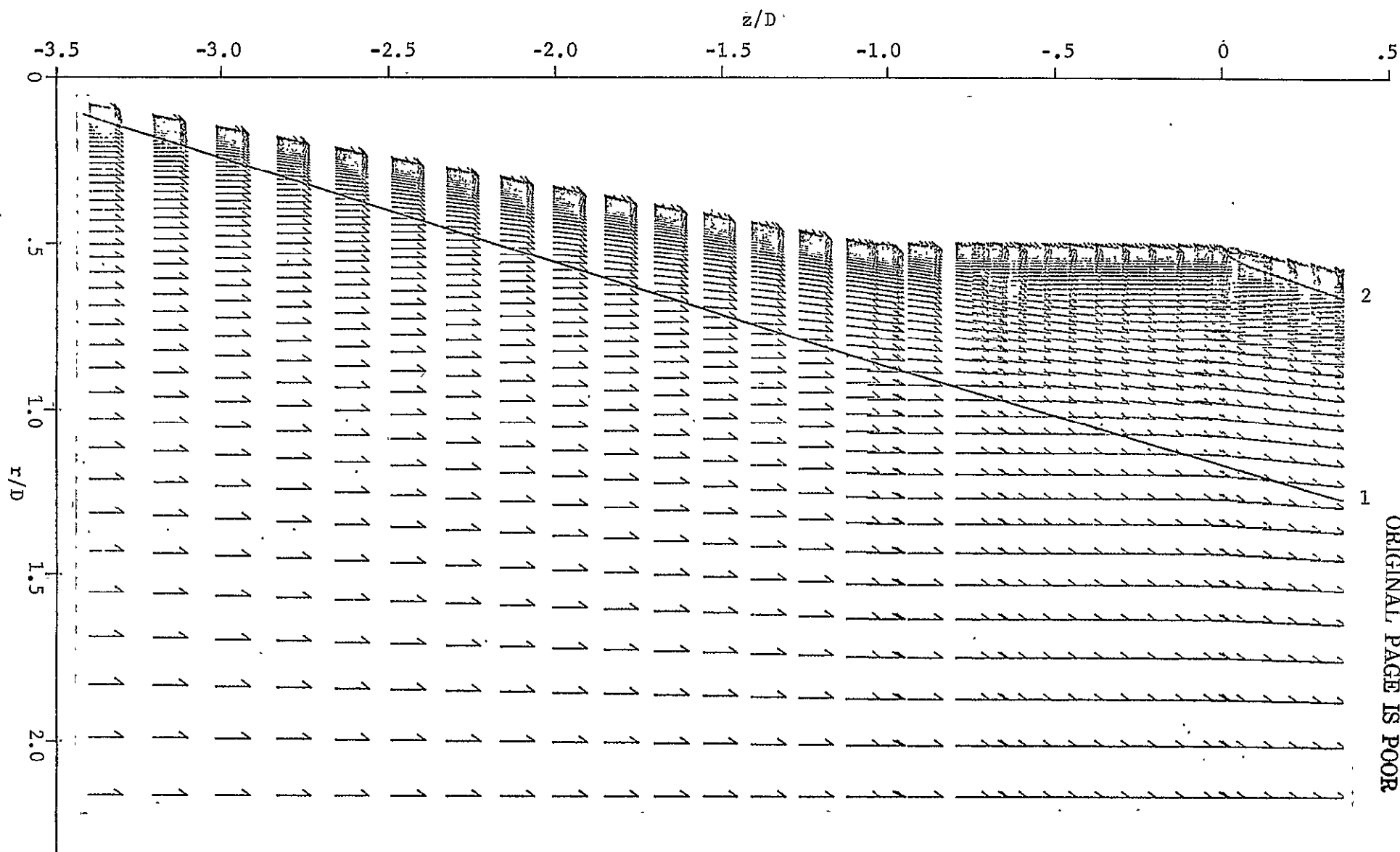


Figure 7. Velocity Vector Plot of the Cone-Cylinder-Flare Flow Field after Three Viscous Iterations.
Curve 1 denotes the cone shock; Curve 2 denotes the flare shock.

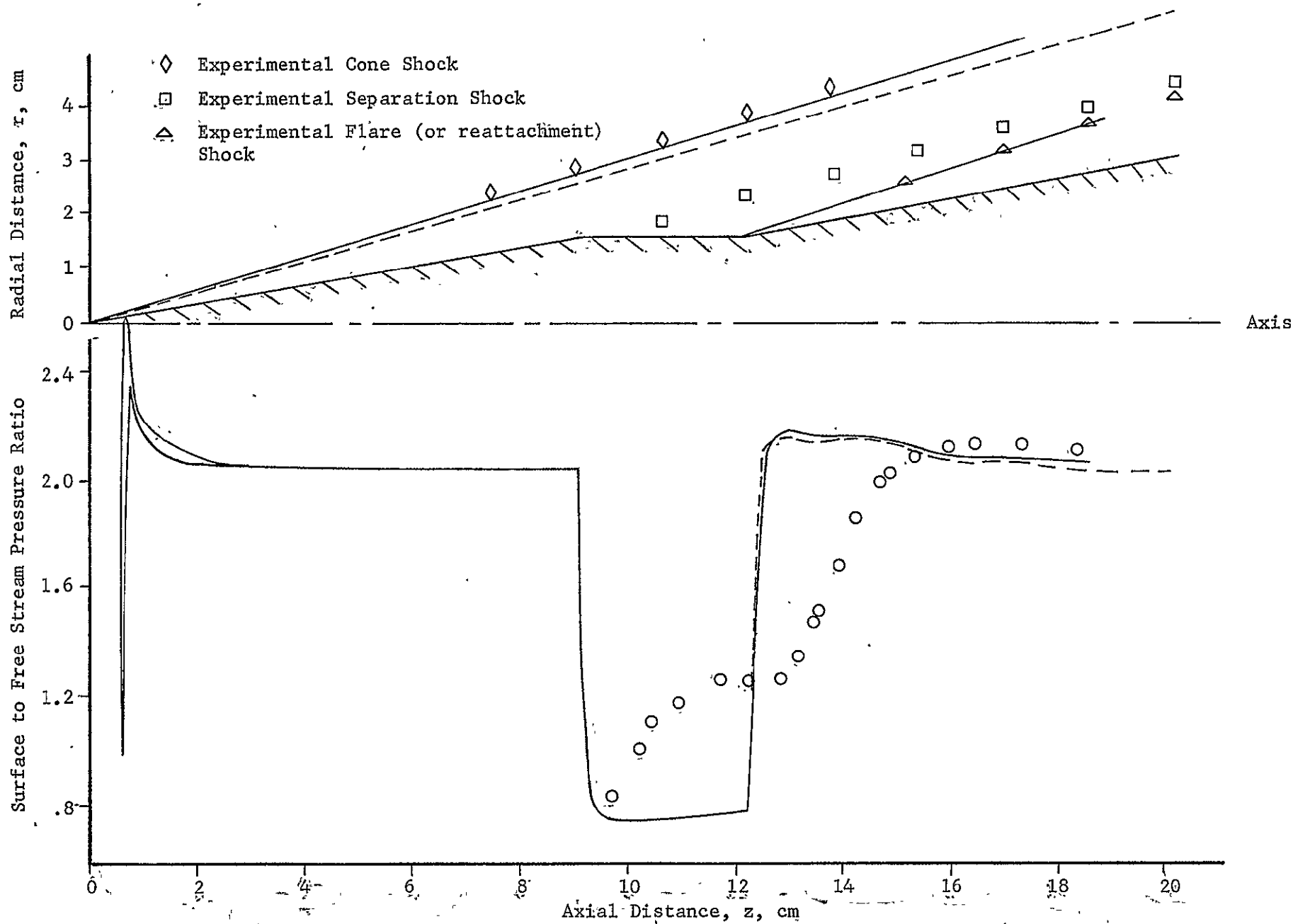


Figure 8. Comparison of Numerical and Experimental Surface Pressure Distributions and Shock loci; $M_\infty = 4.42$, $R_\infty = 1.14 \times 10^5$ cm; solid lines indicate numerical results for first viscous iterate; dashed lines represent inviscid solution or zeroth iterate; cross-hatched line indicates body geometry.

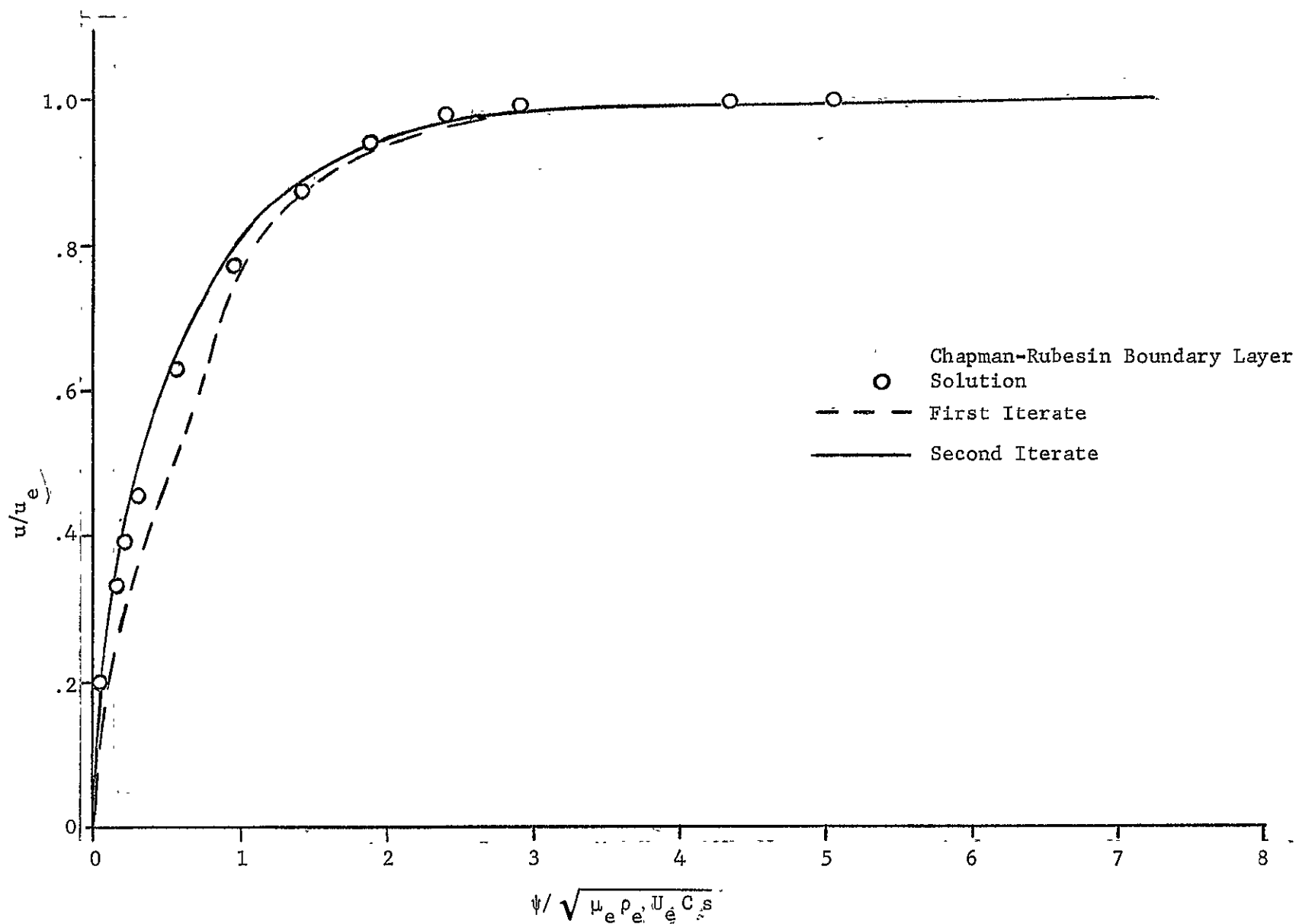


Figure 9. Comparison of Numerically Calculated Boundary Layer Velocity Profiles on the Cone Surface with Boundary Layer Theory.

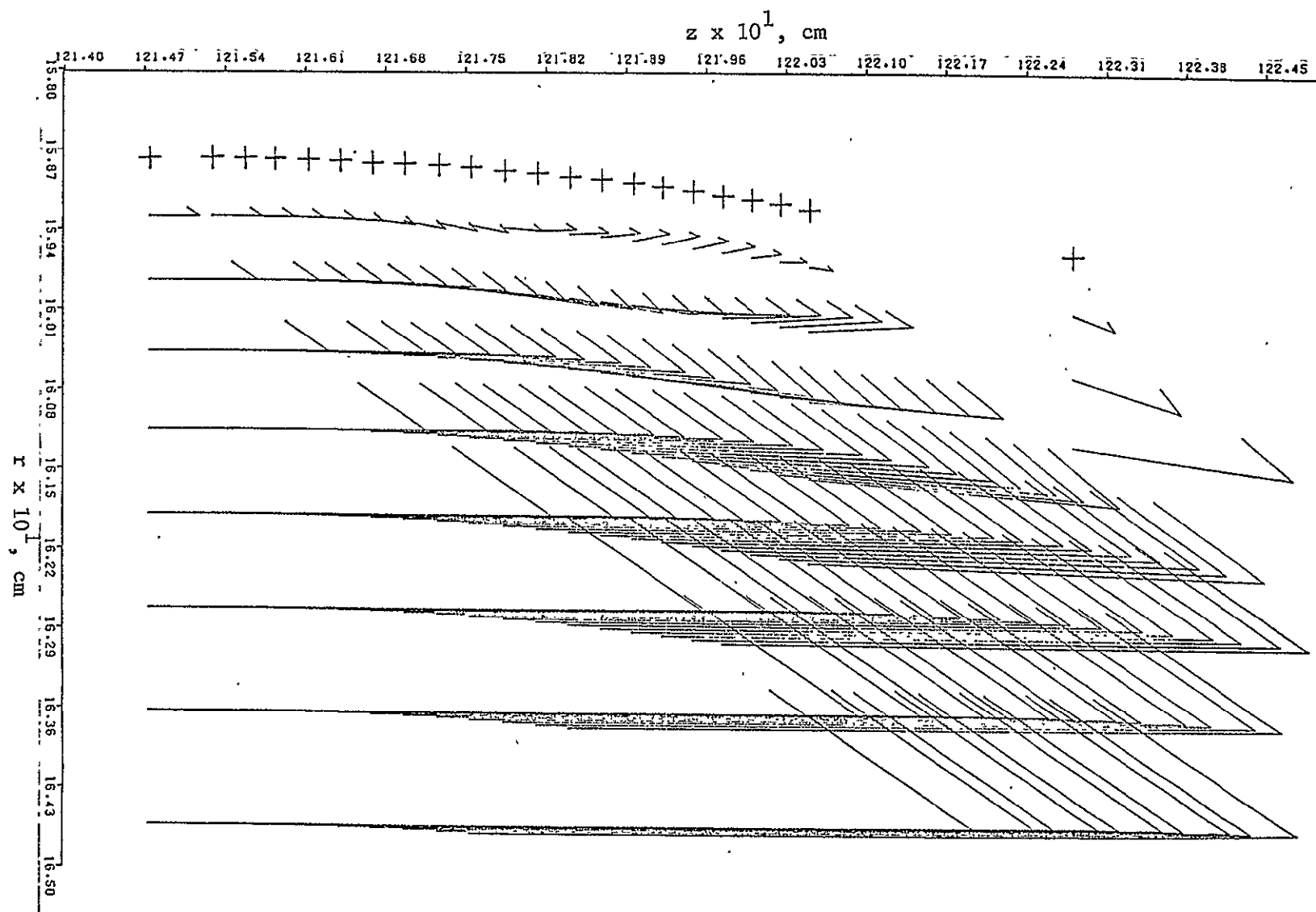


Figure 10. Velocity Vector Plot of the Flow Field in the Neighborhood of the Cylinder-Flare Junction; vectors correspond to numerical data from the third iterate; + symbols indicate the cylinder-flare geometry.

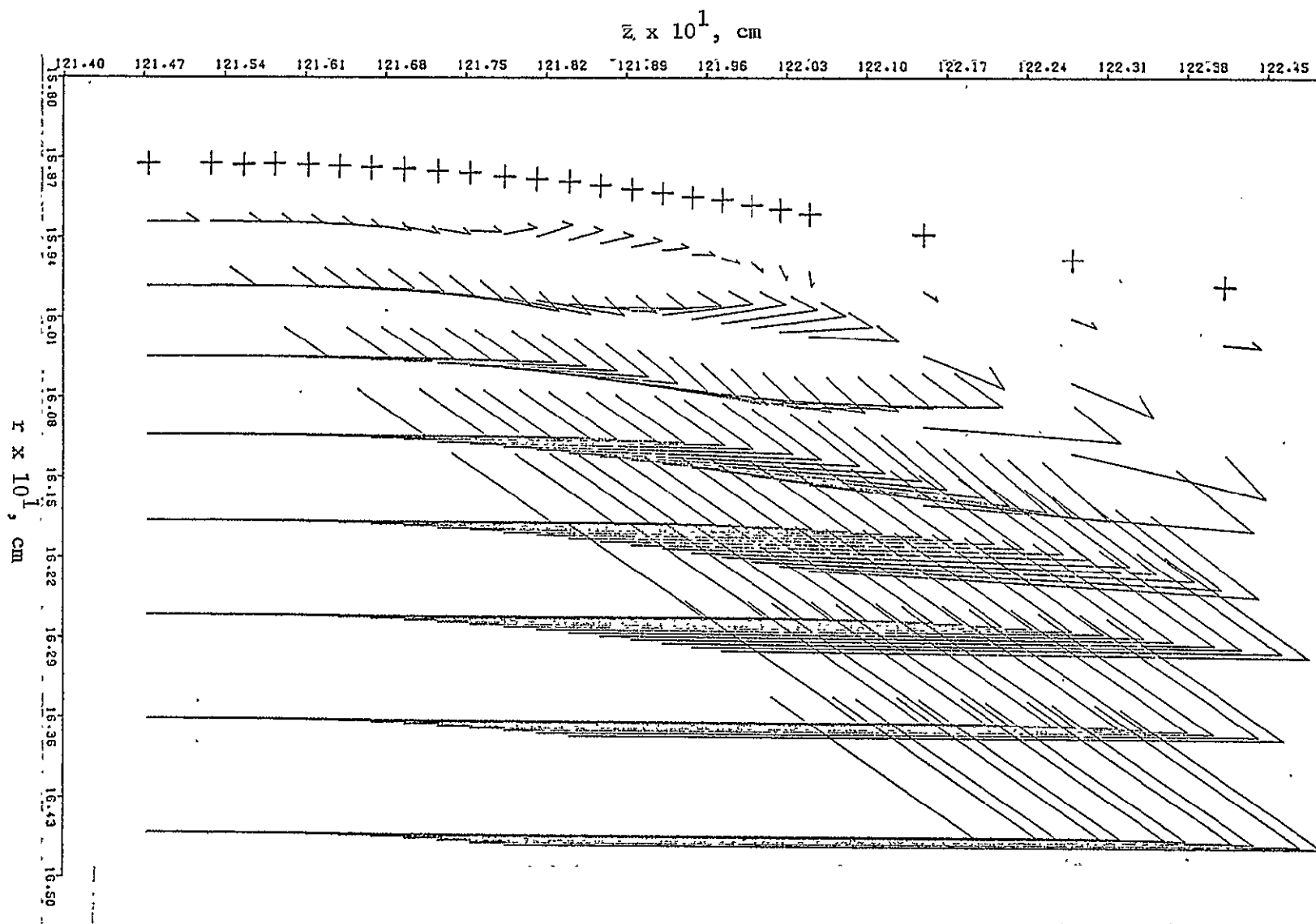


Figure 11. Velocity Vector Plot of the Flow Field in the Neighborhood of the Cylinder-Flare Junction; vectors correspond to numerical data from the fourth iterate; + symbols indicate the cylinder-flare geometry.

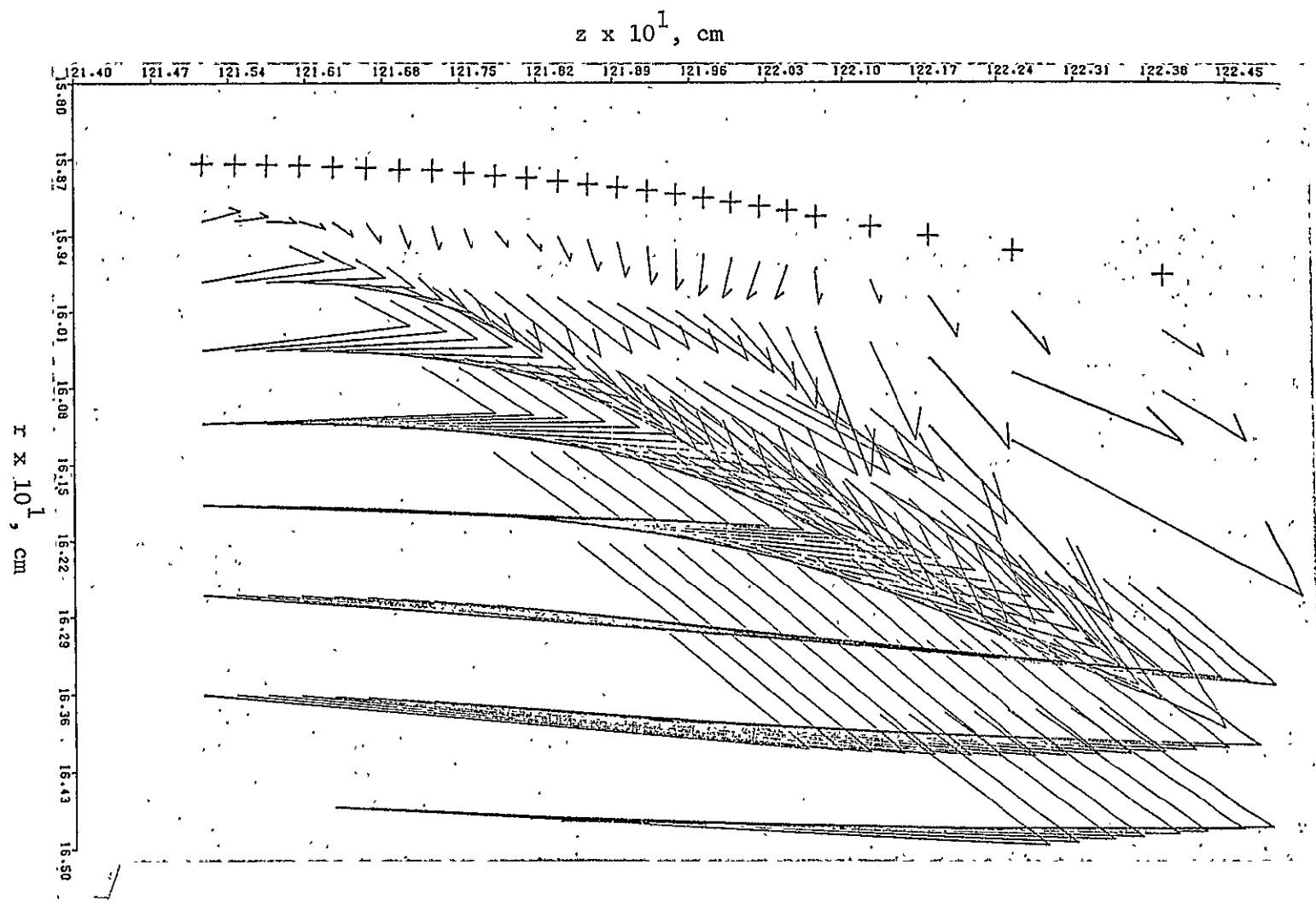


Figure 12. Velocity Vector Plot of the Flow Field in the Neighborhood of the Cylinder-Flare Function; vectors correspond to numerical data from the fifth iterate; + symbols indicate the cylinder-flare geometry.

REPRODUCIBILITY OF THE
ORIGINAL PAGE IS POOR

REFERENCES

1. Trulio, J.G., "Theory and Structure of the AFTON Codes" Technical Report AFWL TR-66-19 (1966).
2. Hayes, W.D., "On Hypersonic Similitude", Quarterly of Applied Mathematics, Vol. 5, pp. 105-108 (1947).
3. Van Dyke, M.D., "A Study of Hypersonic Small-Disturbance Theory", NASA Report 1194 (1954).
4. Walitt, L., Trulio, J.G., and King, L.S., "A Numerical Method for Computing Three-Dimensional Viscous Supersonic Flow Fields About Slender Bodies", NASA SP-228, Analytic Methods in Aircraft Aerodynamics, A Symposium held at Ames Research Center October 28-30, 1969; also NASA CR-1963 (1972).
5. Trulio, J.G., Carr, W.E., and Mullen, J.B., "PUFF Rezone Development", Air Force Weapons Laboratory Report AFWL TR-69-50 (1969).
6. von Neumann, J., and Richtmyer, R.D., "A Method for the Numerical Calculation of Hydrodynamic Shock", J. Applied Physics, 21, p. 232-237 (1950).
7. Kuehn, D.K., "Laminar Boundary-Layer Separation Induced by Flares on Cylinders at Zero Angle of Attack", NASA Technical Report P-146 (1962).
8. Ames Research Staff, "Equations, Tables and Charts for Compressible Flow", NACA 1135 (1953).
9. Pai, S.P., Viscous Flow Theory I - Laminar Flow, pp. 197-201, Van Nostrand, New York (1956).
10. Reference 9, pp. 262-264.
11. Tracy, R., "Hypersonic Flow Over a Yawed Circular Cone", GALCIT Hypersonic Project Memorandum No. 69 (1963).
12. Reference 9, pp. 152-154.
13. Reference 9, pp. 175-179.